Mechanical Engineering

Proceedings of the 7th Baltic Mechatronics Symposium

Tallinn April 8, 2022

Kiviluoma Panu
Kuosmanen Petri
Otto Tauno

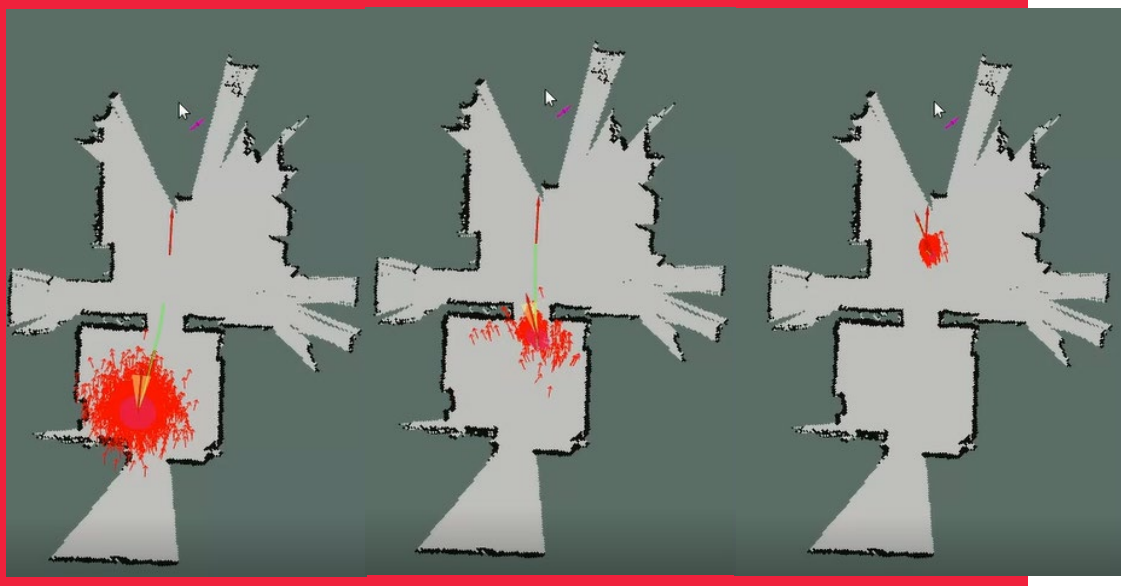

Aalto University
School of Engineering

TAL TECH

Proceedings of the 7th Baltic Mechatronics Symposium

Tallinn April 8, 2022

Kiviluoma Panu
Kuosmanen Petri
Otto Tauno

Aalto University
School of Engineering
Mechanical Engineering

Tallinn University of Technology
School of Engineering
Department of Mechanical and Industrial Engineering

Cover image by Eerik Alamikkotervo, Pejman Habibiroudkenar, Markus Rumjantsev and Vertti Vainio (Project ROSBot

ISBN 978-952-64-9615-3 (pdf)

Abstract

Aalto University, P.O. Box 11000, FI-00076 Aalto www.aalto.fi
TALTECH, Ehitajate tee 5, 19086 Tallinn, Estonia www.ttu.ee

Author
Kiviluoma Panu, Kuosmanen Petri, Otto Tauno

Name of the publication
Proceedings of the 7th Baltic Mechatronics Symposium
Publisher Aalto University School of Engineering
Unit Mechanical Engineering
Field of research Mechanical Engineering
Language English

Abstract

The Baltic Mechatronics Symposium is annual symposium with the objective to provide a forum for young scientists from Baltic countries to exchange knowledge, experience, results, and information in large variety of fields in mechatronics. This year the Symposium was organized in Tallinn in co-operation with Taltech and Aalto University. After two years with virtual meetings due to the ongoing COVID-19, the symposium was organized as face-to-face meeting. The venue of the Symposium was Mectory at Taltech.

The content of the proceedings

1. Autonomous Rescue Vehicle Using 3D Lidar
2. Detection of Ferrite-austenite Transition with the Impedance of an R-L Circuit
3. Hall-sensors in Coupling Condition Monitoring
4. Test Equipment for Curved Aerostatic Bearing
5. Effect of Reused Exhaust Air in Pneumatic System
6. Development of Electromagnetic Unlocking on Container Semi-Automatic Twistlocks
7. People Detection in an Elevator Car Using Computer Vision
8. Electromechanical Multi-material Extruder for Bioprinting
9. Induction Heating of EN 1.4307 Stainless Steel Sheet with Permanent Magnets

In addition, following presentations were also given at the Symposium:

1. TalTech Product development and Robotics student projects - RetroEV and AV shuttle iseAuto. *Hagart Nakkurt*
2. Bending machine service robotization. *Nikita Virunen, Juri Kovaljov*
3. Reaction wall in two months. *Karl Markus Mäesalu*
4. TalTech Participation at Bosch Future Mobility Challenge 2022. *Behzad Mahboubi*
5. Advanced application of the Middleware Services for the Digital Twin of an Autonomous Electric Vehicle Propulsion Drive. *Mahmoud Ibrahim*
6. Methodology for Diagnostics of Energy Storage Systems Based on System Digital Representation. *Rolando Antonio, Gilbert Zequera*
7. Advanced Thermal Management Systems for Electric Machines Using Additive Manufacturing. *Martin Sarap*
8. Additive Manufacturing of Electrical Machines. *Muhammad Usman Naseer*

Keywords Mechatronics, Industrial Internet, Sensors, Actuators, Control
ISBN (pdf) 978-952-64-9615-3
Location of publisher Helsinki
Pages 55

Autonomous Rescue Vehicle Using 3D Lidar

Eerik Alamikkotervo[1, a] , Pejman Habibiroudkenar[1, b] , Markus Rumjantsev[1, c] , Vertti Vainio[1, d] , Alvari Seppänen[1, e] , Panu Kiviluoma[1, f] and Petri Kuosmanen[1, g]

[1] Department of Mechanical Engineering, Aalto University, Finland

[a]eerik.alamikkotervo@aalto.fi, [b]pejman.habibiroudkenar@aalto.fi, [c]markus.rumjantsev@aalto.fi, [d]vertti.vainio@aalto.fi, [e]alvari.seppanen@aalto.fi, [f]panu.kiviluoma@aalto.fi, [g]petri.kuosmanen@aalto.fi

Keywords: ROS, Autonomous navigation, 3D Lidar, Adaptive Monte Carlo Localization

Abstract

Indoor rescue missions can be a challenging task for autonomous navigation as the robot can't rely on external light and the robot must be able to navigate in narrow spaces where distance to the robot is small. In this study an autonomous rescue robot that utilizes only 3D lidar and wheel measurements is developed and the accuracy of navigation in narrow opening is determined in an experimental test. The results propose that the localization of the tested platform is not accurate and robust enough for navigation in rescue environments where space is limited. Accurate results were only obtained in very optimal initial conditions. Also, variation between test runs was large.

Introduction

The application of autonomous vehicles varies from the depth of the ocean to interplanetary space missions such as Mars One. Autonomous vehicles can assist humankind in many aspects, such as exploration, self-driving cars or in some cases as rescue robots. Nowadays rescue robots are used as a means for surveillance and information gathering such as DJI Mavic 2 Enterprise Dual drone. But in some cases, the rescue robot assists with rescuing tasks, for example, Thermite RS2-T2 is a remote-controlled robot that can handle distinguishing fire within 300 meters. However, due to the complexity of the environment and unpredictable dangers, the next step of the rescue missions is autonomic operation [1].

Research for navigating in large indoor rescue environments [2], accuracy of 3D lidar mapping outdoors [3, 4] and accuracy of optical and radio beacon triangulation systems [5, 6] exists. However, the research for autonomous navigating indoors with 3D lidar in tight spaces, where the distance between the robot and obstacles is small, is not yet comprehensive. Additionally, multiple sensors are usually utilized in autonomous navigation including lidar scanners, inertial measurement units, depth cameras and sonars [7]. In this study only one 3D lidar and wheel odometry are used to avoid the issues created by sensor fusion [8] and to make the system completely independent of external light.

Autonomous navigation in any environment includes four main steps: mapping of the environment, localization of the robot, planning a path from initial pose to the target pose and following this path. In each of these steps the accuracy is mostly affected by the accuracy of the distance sensor, the accuracy of the odometry and the performance of the localization and path finding algorithms used. In this study Velodyne VLP-16 3D lidar was used for distance measurements, wheel encoders for odometry and Robot Operating System (ROS) navigation stack packages for localization and path finding. ROS navigation stack packages utilized Blackwellized Particle Filter for simultaneous localization and mapping (SLAM) [9], Dijkstra and Dynamic Window Approach for path planning [10, 11] and Adaptive Monte Carlo Localization for localization (AMCL) [12].

Methods

System description. The development platform is a differential drive mobile robot (Fig. 1), that is steered based on the speed difference between the driving wheels. The speed of the wheels is measured with hall sensor encoders that have resolution of 12°. The environment is observed with a Velodyne VLP-16 3D lidar. The width of the robot is 82 cm and height 60 cm, which is a reasonable size for robot doing rescue missions.

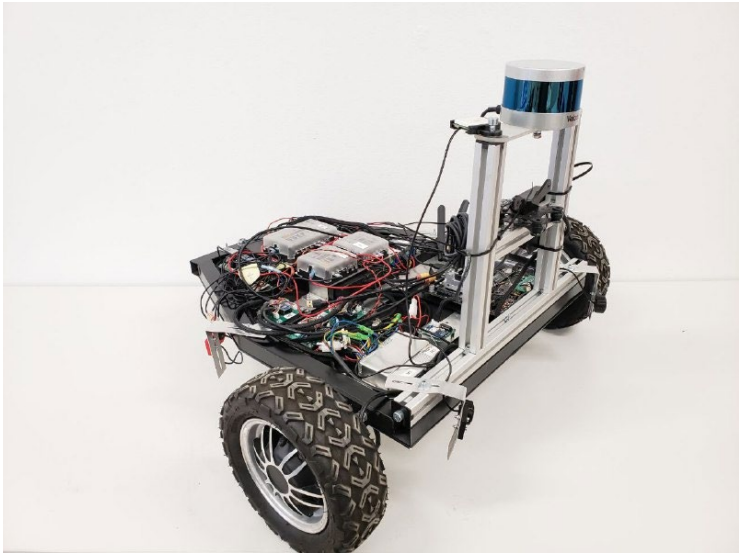

Figure 1. The development platform that utilizes 3D lidar and wheel odometry.

The hardware and software nodes of the system are presented in Fig. 2. Velocity commands and measured velocities are transferred between the motors and the software via Arduino microcontrollers. The *wheel_odom*-node estimates the change in robot position (odometry) based on measured wheel velocities and then feeds it to the navigation stack. The lidar measurement data is processed to point cloud in *velodyne*-node and then compressed into 2D laser scan in the *pointcloud_to_lasercan*-node. The map of the environment is provided from *map_server*-node and

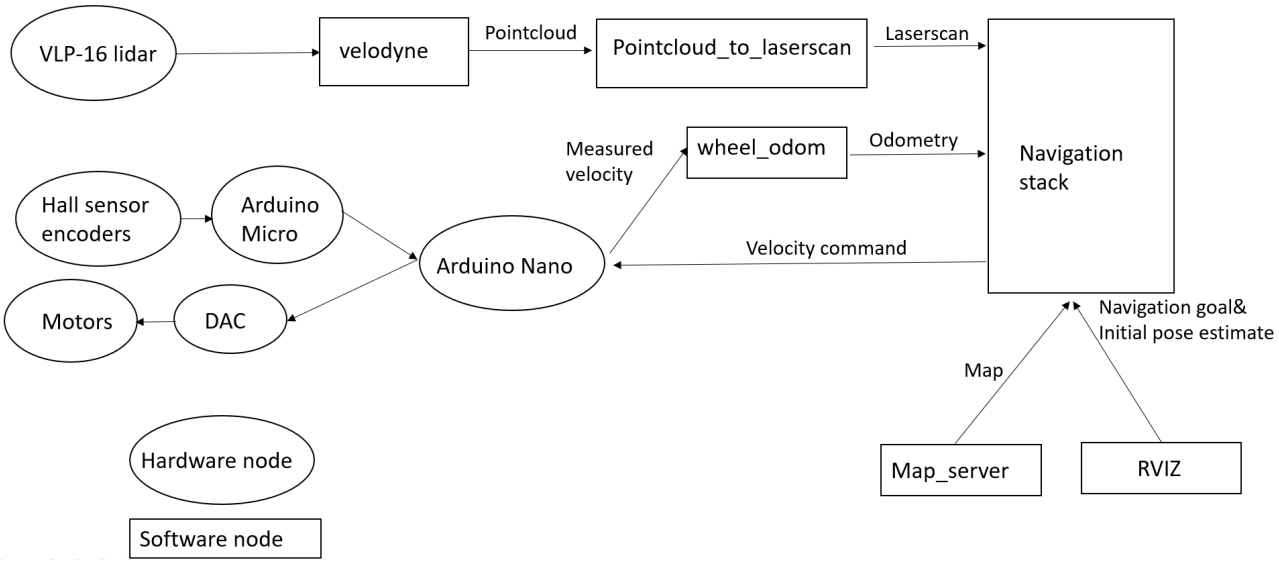

Figure 2. System hardware and software nodes.

the initial position estimate and navigation goal are provided from RVIZ graphical interface. Based on this data the navigation stack localizes the robot, plans a path, and sends the required velocity commands to the wheels to safely reach the target position in the map. All the software nodes run inside ROS.

Mapping process. The environment where the robot moves is mapped before performing autonomous navigation. During the mapping process the robot is driven manually around the space and SLAM algorithm estimates the current position of the robot and then measures distance of the objects from the robot to produce a map. The current position is estimated based on the measured rotation of the wheels (wheel odometry) and laser scan matching. The distance to the obstacles is measured with the 3D lidar. The map is then saved as an occupancy grid where each pixel has a value between 0-100. 0 means completely free and 100 completely occupied. The mapping is performed using ROS package *gmapping.*

Because the robot can only move in the 2D plane, it is desirable to produce a 2D map where any object that is below the highest point of the robot is seen as an obstacle. To achieve this goal the 3D point cloud produced by the 3D lidar is compressed using ROS package *pointcloud_to_laserscan.* The output is 2D scan that registers an obstacle if there is an obstacle in any height on the measurement range. In comparison, 2D lidar would only register obstacles that are in the measured 2D plane. Any obstacle below or above that level is not registered. The difference is illustrated in Fig. 3. Ability to sense obstacles with varying heights is critical when navigating in an environment where space is limited.

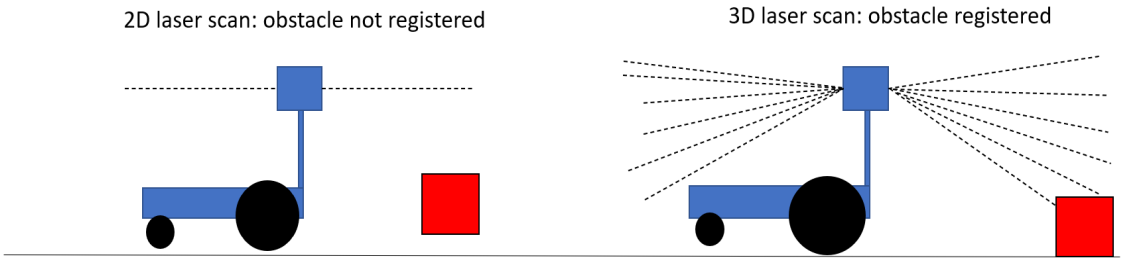

Figure 3. Obstacle detection of 2D lidar and 3D lidar.

Navigation process. Autonomous navigation process includes multiple steps. First the robot needs to localize itself on the map. This is done by comparing the measured laser data and the provided map and utilizing wheel measurements using Adaptive Monte Carlo Localization algorithm (ROS package *amcl*). Second, a goal position should be provided so that a path plan from the current position to the desired position can be formed. The local path planner (ROS package *local_planner*) utilizes Dynamic Window Approach [8], and the global path planner (ROS package *global_planner*) utilizes Dijkstra algorithm [9]. The global planner makes a global plan how to get from the starting pose to the target pose. The local planner takes in a small part of the global plan and tries to complete it while avoiding any obstacles. The local planner can plan the path around obstacles even though they are not represented in the original occupancy grid map. Finally, the robot needs to link the global plan and local plan together and follow the planned path based on the odometry and laser scan data provided. For this stage ROS package *move_base* is utilized. It takes the estimated initial location and desired path as input and sends drive commands to the wheels. The navigation process is presented in Fig. 4.

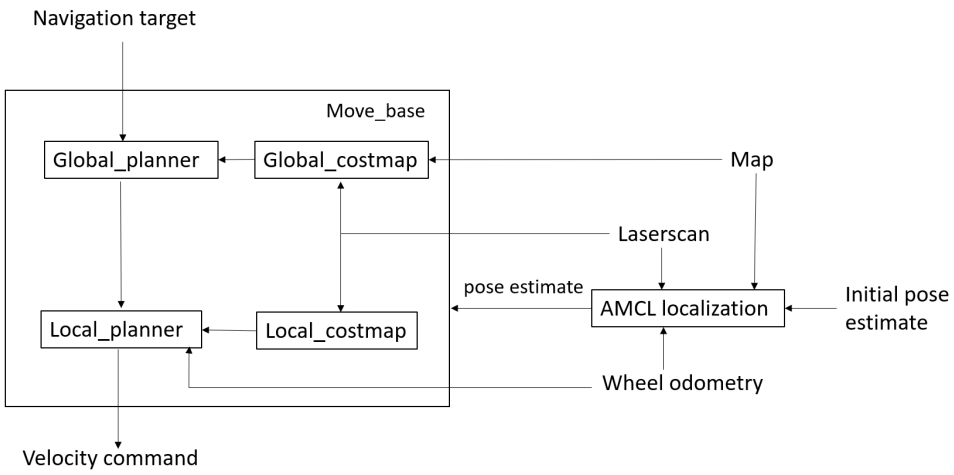

Figure 4. Navigation process using AMCL localization and move_base.

Testing. Main objective of the testing is to obtain the accuracy of the autonomous navigation. The setup will be an opening with easily changeable width *L*. This test setup is illustrated in Fig. 5. The testing is conducted in an inside environment with a flat floor to minimize outside interference with the test results. The robot is placed in the front of the opening and then a navigation target is placed on the other side of the opening. The opening size is then decreased in steps until the robot can't navigate through to obtain the accuracy of the navigation. The robot driving speed during the experiment will be below 0.5 m/s to allow the 3D lidar to collect enough data points from the environment and localize the robot as accurately as possible. Before the test a map of the test environment is produced using the mapping process presented previously.

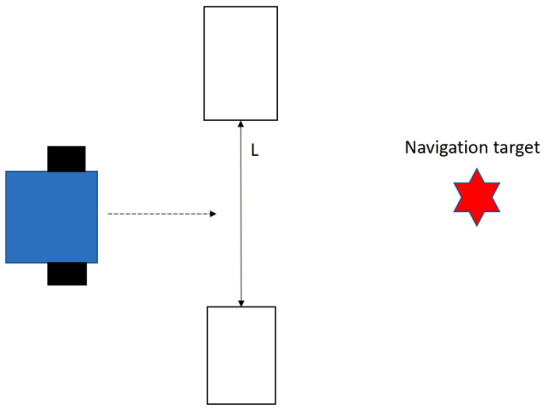

Figure 5. Test set up. L is the width of the opening.

Results

In the experiments the repeatability of the navigation was too poor to present any credible estimate of the navigation accuracy. If the probabilistic AMCL pose estimate converged accurately the robot could navigate through openings with width of only 90 cm (8 cm extra space), but in the same test setup the robot failed to navigate through openings up to size of 130 cm if the AMCL pose estimate was inaccurate. The localization performance varied drastically even with identical starting positions and navigation target. This issue is further explained in the discussion. However, in general the navigation succeeded with higher percentage as the opening size was increased because lower localization accuracy was needed. As conclusion, the test propose that 90 cm (110% of test robot width) is the upper limit of the navigation accuracy with optimal localization performance, but the AMCL algorithm localization performance varied significantly between test runs. The navigation parameters that were used in the experiment are presented in Table 1.

Table 1. Navigation parameters used in the test.

Laser scan parameters	**Costmap parameters**	**Trajectory Planner parameters**
Scan range: 0.4…10.0 m	Obstacle range: 2.5 m Raytrace range: 3 m	Max translation velocity: 0.3 m/s
Scan time: 0.33 s	Robot radius: 0.4 m	Max rotation velocity: 0.4 rad/s
Scan angle 360°	Inflation radius: 0.2 m	Acceleration limit translation: 0.2 m/s^2
Scan height: 0.1…0.7m (from ground level)	Local costmap: Use rolling window, width 6 m, height 6 m	Acceleration limit rotation: 0.2 rad/s^2

Discussion

The accuracy of the navigation is mostly defined by the accuracy of the localization and path planning and the ability to follow the planned trajectory. During testing the localization uncertainty was found to be the largest error source out of these factors. The position estimate array converged on average to circle with diameter of around 50 cm (Fig. 6) and the estimated heading of the robot could drift up to tens of degrees from the actual heading. The error in orientation increases if the robot rotates in place excessively because the wheel odometry performs poorly in rotation. The variation in localization between test runs was large, but generally the longer the robot moved in the environment the better was the position estimate (Fig. 6). Knowing that the robot is inside an estimated 50 cm circle with high probability would be feasible for navigating in large spaces but not for narrow openings in limited indoor environment.

The map quality is also crucial as it is the reference point for the localization. However, it was relatively easy to produce good quality maps if the mapping speed was low and excess rotation of the robot was avoided. The map presented in Fig. 6 was produced with one back and forth drive through the opening. The walls are straight and there are no duplicate reflections of the wall (same wall mapped to two different positions with small offset). The map resolution is only 5 cm, but it is still magnitude smaller than the localization performance so it should not be a bottle neck.

Implementation of inertial measurement unit (IMU) alongside 3D lidar and wheel measurements could improve the accuracy of the localization as it can compensate the weakness of wheel odometry in rotation [13]. Additionally, increasing the wheel encoder resolution (current 12°) could improve the accuracy of the wheel odometry and thus improve the accuracy of the localization, but the improvements would be limited as encoder alone cannot account for the wheel slip.

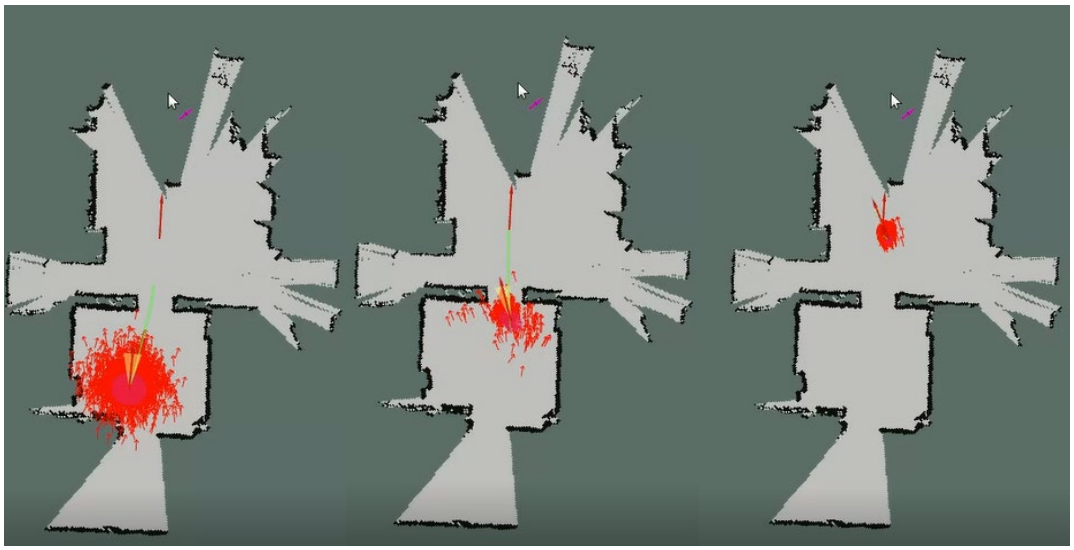

Figure 6. Localization performance during test run. The pose estimate is presented as pose array (red arrows) that converges as robots moves. The green line is planned path and the single red arrow is the navigation target.

References

[1] Liu, J., Wang, Y., Li, B. *et al.* Current research, key performances and future development of search and rescue robots. *Front. Mech. Eng. China* 2**,** 404–416 (2007). https://doi.org/10.1007/s11465-007-0070-2

[2] M. Menna, M. Gianni, F. Ferri and F. Pirri, "Real-time autonomous 3D navigation for tracked vehicles in rescue environments," 2014 IEEE/RSJ International Conference on Intelligent Robots and Systems, 2014, pp. 696-702, doi: 10.1109/IROS.2014.6942634.

[3] Haala N, Peter M, Kremer J, Hunter G. Mobile LiDAR mapping for 3D point cloud collection in urban areas—A performance test. Int. Arch. Photogramm. Remote Sens. Spat. Inf. Sci. 2008 Jul 3;37:1119-27.

[4] Marek P, Philippe G, Rasmus A, 2018, Mapping forests using an unmanned ground vehicle with 3D LiDAR and graph-SLAM,Volume 145,Pages 217-225,ISSN 0168-1699,https://doi.org/10.1016/j.compag.2017.12.034.

[5] Básaca-Preciado LC, Sergiyenko OY, Rodríguez-Quinonez JC, García X, Tyrsa VV, Rivas-Lopez M, Hernandez-Balbuena D, Mercorelli P, Podrygalo M, Gurko A, Tabakova I. Optical 3D laser measurement system for navigation of autonomous mobile robot. Optics and Lasers in Engineering. 2014 Mar 1;54:159-69. https://doi.org/10.1016/j.optlaseng.2013.08.005.

[6] S. Park and S. Hashimoto, Autonomous Mobile Robot Navigation Using Passive RFID in Indoor Environment, in IEEE Transactions on Industrial Electronics, vol. 56, no. 7, pp. 2366-2373, July 2009, doi: 10.1109/TIE.2009.2013690.

[7] M. B. Alatise and G. P. Hancke, A Review on Challenges of Autonomous Mobile Robot and Sensor Fusion Methods, in IEEE Access, vol. 8, pp. 39830-39846, 2020, doi: 10.1109/ACCESS.2020.2975643.

[8] Ren C Luo, Michael G Kay, Multisensor Integration And Fusion: Issues And Approaches, Proc. SPIE 0931, Sensor Fusion, (9 August 1988); https://doi.org/10.1117/12.946646

[9] Ayoade, Femi & Sagor, Jane & Hasan, Md & Oluwatobi, Adekunle. (2021). Comparison of Two SLAM Algorithms Provided by ROS (Robot Operating System). 1-5. 10.1109/INCET51464.2021.9456164.

[10] ROSwiki. Base_local_planner. [Read 14.3.2022]. Available: http://wiki.ros.org/base_local_planner

[11] ROSwiki. Global_planner. [Read 14.3.2022]. Available: http://wiki.ros.org/global_planner

[12] ROSwiki. AMCL. [Read 6.4.2022]. Available: http://wiki.ros.org/amcl

[13] J. Shen, D. Tick and N. Gans, "Localization through fusion of discrete and continuous epipolar geometry with wheel and IMU odometry," Proceedings of the 2011 American Control Conference, 2011, pp. 1292-1298, doi: 10.1109/ACC.2011.5990946.

Detection of Ferrite-austenite Transition with the Impedance of an R-L Circuit

Oskari Räsänen[1,a], Aku Mustalahti[1,b], Andreas Blomfelt[1,c], Panu Kiviluoma[1,d] and Petri Kuosmanen[1,e]

[1] Department of Mechanical Engineering, Aalto University, Finland

[a]oskari.rasanen@aalto.fi, [b]aku.mustalahti@aalto.fi, [c]andreas.blomfelt@aalto.fi, [d]panu.kiviluoma@aalto.fi, [e]petri.kuosmanen@aalto.fi

Keywords: Curie temperature, Curie point, stainless steel, inductance, impedance, ferrite-austinite

Abstract

In the metal manufacturing industry, the measurement of the temperature of the materials processed is one of the most important aspects. In the high temperature processes, there are challenges related to phenomena such as severe oxidation of surfaces, the emissivity coefficient of electromagnetic radiation and the durability of measurement tools. Using multiple measuring systems can produce more accurate and reliable results. In some metals and alloys magnetic properties of the materials change significantly with phase changes around the Curie temperature. In ferritic steels particularly, transition from ferrite to austenite happens near the temperature of change from ferromagnetic to paramagnetic. This research examines the possibility of detecting the loss of ferromagnetic properties in the change of impedance in an electromagnetic coil with a heated ferritic stainless-steel core. The impedance change in the Curie temperature range was found to be clearly visible in the collected data, suggesting that this type of measurement is a functional method for finding the Curie point of ferromagnetic materials.

Introduction

Magnetic susceptibility, permeability and remanence of ferritic stainless-steel drop significantly along transformation from ferritic to austenitic microstructure. This is largely due to the paramagnetic nature of austenite. This transformation occurs around the Curie temperature, which ranges from 650 to 750°C for most steels [1, 2]. The change does not happen instantly, but over a range of temperatures where the ferromagnetic behavior decreases quickly until it disappears. The change from ferromagnetic to paramagnetic behavior is partly caused by the transformation of the crystal structure of the steel from a ferritic body-centric cubic structure to an austenitic face-centric cubic one. The magnetic moments that cause the ferromagnetic behavior in the ferritic phase disappear. Ferromagnetic materials can cause an increase in the local magnetic flux if they are being magnetized. This means that the lines of the magnetic field are being concentrated in the ferromagnetic material in relation to the surrounding regions. Paramagnetic materials do not exhibit this type of behavior in a significant manner. In this study, a method that takes advantage of this transformation and the consequent change in magnetic properties is proposed to estimate the moment the steel has reached its Curie temperature. [3, 4, 5]

The proposed method is based on the use of a resistor-inductor (R-L) circuit to detect the ferrite-austenite transition of a ferritic stainless-steel strip. Inductance of a coil is mostly affected by the shape of the magnetic field. This is governed by both the geometry of inductor itself and the permeability of the core material. A ferromagnetic core orients magnetic field lines, potentially increasing inductance by a factor of thousands [6]. In the measurement presented in this study, the stainless-steel sheet acts as the core of a flat coil placed on top of it. When the phase transition in the sheet occurs, there should be a clear change in the magnetic performance of which will in turn change the voltage drop measured voltage the coil.

Methods

Theory. A conductor loop placed on the steel sheet in the oven has resistance, inductance, and capacitance. Of these, theoretically only resistance is temperature dependent [6]. The steel sheet acts as a core for the inductor, highly increasing its inductance. The hypothesis is that the ferrite-austenite transition results in a drop of permeability of the sheet-core and a subsequent drop in inductive impedance of the circuit. Rising temperature and oxidation of the conductor are also expected to cause a rise in resistance. Surface effect is expected to stay constant.

A series R-L circuit is driven by 20 MHz alternating current (AC) set at 5V peak-to-peak supplied by a function generator. The ratio of voltages over the entire series R-L circuit and only the resistor is used to find their relative impedances. Furthermore, voltage-current phase difference is governed by the ratio of inductive to capacitive impedance at a given frequency, but this is not employed in this study as capacitance is expected to be negligible [6].

Impedance of a ferromagnetic core does not grow linearly with frequency. At low frequencies (Hz), resistance is the dominating factor. At medium frequencies, ferromagnetic hysteresis effects dominate. These hysteresis effects are of present interest. At high frequencies, Eddy currents are formed in the material.

The overall impedance of a circuit is given by the equation

$$Z = \sqrt{R^2 + (X_L - X_C)^2}, \quad (1)$$

Where X_C and X_L are the reactance caused by the capacitance and inductance in the circuit. Coil impedance was determined with the formula:

$$Z_{coil} = \frac{(V_{supply} - V_{Rref}) \cdot R_{ref}}{V_{Rref}} \quad (2)$$

Where Z_{coil} is the coil impedance, V_{supply} is the supply voltage, V_{Rref} is the voltage measured over the reference resistor and R_{ref} is the reference resistor resistance. In the series circuit, coil was in higher and resistor in lower potential.

Test setup. The coil placed in the oven must withstand the high temperatures for several minutes. As Single-wire copper conductors can withstand oxidation in high temperatures, a single-wire 2,5mm^2 copper conductor was used in the test. A flat coil was turned using a jig so that none of the turns were in contact with one another. Additionally, one layer of glass fiber was put between the coil and the steel sheet for insulation. Note that single-wire conductors still suffer significantly from the skin effect. The turned copper conductor is seen in Fig. 1.

Figure 1. The single-wire copper coil positioned on a steel sheet with glass fiber in-between for insulation.

A K-type thermocouple was planted under the sample sheet to obtain temperature measurements to be used as a reference value for the impedance change. Both the voltage drop over the parts of the RL-circuit and the thermal readings from the thermocouple were collected digitally with a data logger and compared to the elapsed time during the tests. As the Curie temperature of this stainless steel is known from literature as 650-750°C, the point in the thermocouple data is used to assess the point in time when the Curie point is reached [1, 2]. This time point was then used to examine the changes in the voltage loss over the circuit and how they matched the thermocouple data.

Voltages over parts of the circuit were measured from capacitor-smoothed single-diode rectifiers with bleed resistors. Input impedance of the data collection device is so high that the bleed resistors could be chosen with high enough resistances as to produce negligible error.

The oven, which can be seen in Fig. 2, used in the final testing is a design based on heating by electrical resistors. It is meant for the heating of metals to high temperatures for casting and heat treatment processes in small workshops and laboratories. Therefore, the insulation of the oven is effective, and the fluctuations of the temperature are small. The oven also has precise adjustments and controls for the selection of the temperatures, making it a suitable tool for the testing purposes of this study. An opening in the bottom of the oven acts as a route to insert the necessary cables for the testing coil and a thermocouple into the oven.

Figure 2. The oven used in the testing.

Results

Initial test. In the initial testing, voltage was measured both over the coil and the entire circuit. Ferritic and austenitic stainless steels were brought to touch the coil, increasing impedance and thus, voltage drop over the coil. Originally, a frequency of around 5 MHz was calculated to give inductive impedance of the same order of magnitude as the resistor's resistance. It was quickly discovered however, that a frequency of around 20 MHz gave much more pronounced changes in voltage. The coil used in these tests was a thermocouple wire that was wound into several loops stacked on top of each other, producing a short cylindrical shape.

With medium frequency, around 10% change in voltage loss over the coil was measured with the coil placed on a metal sheet. Aluminum also produced a noticeable effect, likely due to its high conductivity and consequent eddy currents.

Based on the results from the preliminary testing phase, it was decided that the relative effect of the coil and core needed to be increased. Thus, the coil would need to be wound as flat and close to the steel sheet as possible, and with more turns. To create this coil shape, a jig was made that allowed for the conductor to be wound into a flat spiral shape consistently.

Final tests. The results from final tests can be seen in Fig. 3 and Fig. 4. Fig. 3 represents the temperature dependence of impedance when the steel is heated from 200°C to 800°C, and Fig. 4 represents the cooling of the steel from 800-200 °C. Note that both the impedance and temperature were collected with time stamps and only later plotted one against another.

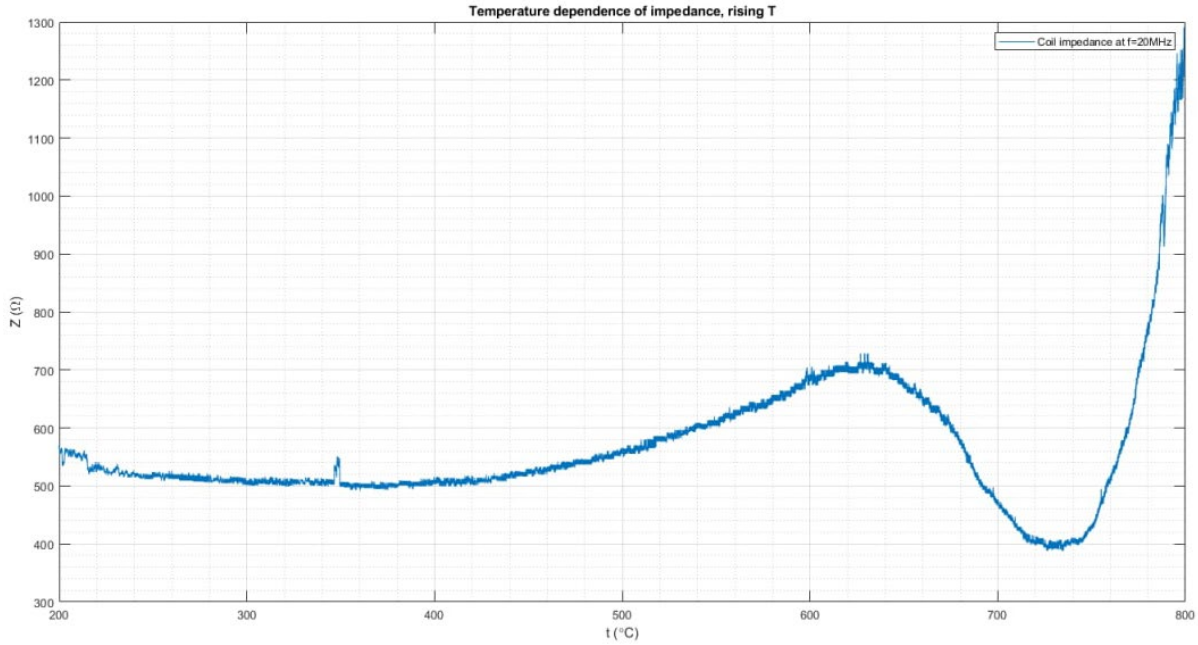

Figure 3. The temperature dependence of impedance when the temperature is rising.

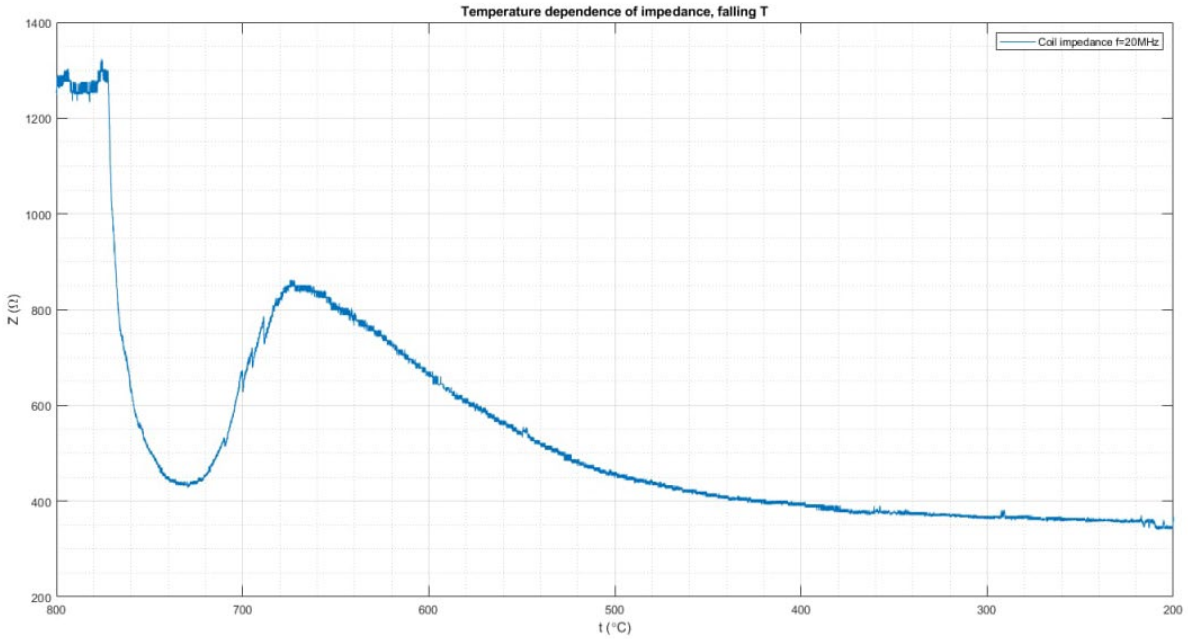

Figure 4. The temperature dependence of impedance when the temperature is falling.

Between 200-650°C in the heating of the steel, the impedance rose slowly. This was due to the resistance of the conductor increasing when the temperature rise. As seen around 650°C, there was a noticeable drop in the impedance over the coil as the steel approached its known Curie temperature. The impedance change was therefore likely caused by the austinite-ferrite transformation of the steel. The austinite-ferrite transformation occurs over the intercritical temperature range and not perfectly suddenly, as the diffusion of carbon in the crystal structure takes time and energy [1]. Thus, the impedance change was not instant, but happened gradually between around 650-730°C. At around 730°C, the derivative of the impedance was 0. This could be interpreted as the Curie temperature, as at this point the steel had a fully austenitic structure, had lost all its permanent magnetic properties, and thus the coil has no inductance contributing to the impedance. The rise of impedance after 730 °C is attributed to the drastic increase in resistance of the conductor with the rising temperature. Temperature of the copper coil likely also differs from the temperature of the steel.

When cooling the steel, the same pattern can be seen reversed. The derivative of the impedance was 0 at around 730 °C, confirming the Curie temperature being the same as in the heating. Note that the cooling occurred much faster than the heating and there is some difference in the temperatures when the change occurs. This is likely caused by the different change rates of the temperature as well as by the transition processes between ferrite and austenite that are not exactly the same during both cooling and heating [1]. This also likely relates to the absolute value of the impedance differing between the heating and cooling.

Discussion

Based on the findings from the testing that was carried out, the change in voltage from stainless steel strips in heat treatment ovens can be measured using a flat coil to detect changes in the voltages induced across it. To achieve reliable results, the parameters of the current that is used in the RL circuit must be selected correctly. The use of excessively high frequencies in the preliminary testing resulted in unwanted electromagnetic phenomena that interfered with the measurements.

Practical industrial applications for this measuring technique can be found in heat treatment and similar processes, where the temperature of the material needs to be measured. The point of time when the Curie point is reached can be used as a reference for the calibration of other measurement systems that might be used, such as pyrometers, for example. Alternatively, many processes can be carried out in the Curie temperature range to alter the properties of steels. For many steels, the temperatures used in hardening processes that involve quenching, the quench temperature is very close to the ferrite-to-austenite phase transition point and therefore also close to the Curie temperature. This type of electromagnetic measurement can be a cost-effective solution for a quick and relatively simple assessment if the required temperatures are reached. For added reliability in such processes, this method of coil measurement can easily be added as a secondary method of measurement to reduce uncertainties during the manufacturing.

Effect of the temperature-dependent resistance of the copper should be accounted for by periodically measuring direct current resistance, which then is subtracted from total measured impedance.

If this method would be used in practice, the definition of the exact Curie point would have to be defined by the users of the method. For instance, in the tests of this research, the Curie point was defined as the point when the derivative of the impedance becomes 0 the first time after the austenite-ferrite transformation. This way the user can consistently find a point to reference to instead of an interval that the austenite-ferrite transformation occurs in.

References

[1] J. Charles, J. D. Mithieux, P. O. Santacreu, and L. Peguet, “The ferritic stainless family: The appropriate answer to nickel volatility?,” *Rev. Metall. Cah. D’Informations Tech.*, vol. 106, no. 3, pp. 124–139, 2009, doi: 10.1051/metal/2009024.

[2] K. Ara, M. Yamada, and T. Kakuta, “MAGNETIC CHARACTERISTICS OF FERROMAGNETIC MAGNETIC CHARACTERISTICS OF FERROMAGNETIC STAINLESS STEEL,” *JAERI-M*, vol. 86, no. 181, 1986.

[3] M. Y. Belomyttsev, E. I. Kuz’Ko, P. A. Prokof’Ev, and T. D. Sulyaev, “Magnetometric analysis to examine critical temperatures and structural state of the 13%-cr steels,” *Izv. Ferr. Metall.*, vol. 60, no. 9, pp. 732–738, 2017, doi: 10.17073/0368-0797-2017-9-732-738.

[4] J. Childress, S. H. Liou, and C. L. Chien, “Magnetic Properties of Metastable 304 Stainless Steel With Bcc Structure,” *Le J. Phys. Colloq.*, vol. 49, no. C8, pp. C8-113-C8-114, 1988, doi: 10.1051/jphyscol:1988843.

[5] W. Zhu, “Electromagnetic Techniques for On-line Inspection of Steel Microstructure,” 2013.

[6] I. . Grant and W. . Phillpis, *Electromagnetism*. John Wiley & Sons, Inc., 1990.

Hall-sensors in Coupling Condition Monitoring

Olli-Eemeli Sirviö[1,a], Aditya Prakash[1,b], Amith Nair[1,c], Markus Määttä[1,d], Panu Kiviluoma[1,e], Petri Kuosmanen[1,f]

[1] Department of Mechanical Engineering, Aalto University, Finland

[a]olli-eemeli.sirvio@aalto.fi, [b]aditya.prakash@aalto.fi, [c]amith.nair@aalto.fi, [d]markus.s.maatta@aalto.fi, [e]panu.kiviluoma@aalto.fi, [f]petri.kuosmanen@aalto.fi

Keywords: coupling, condition monitoring, Hall-sensor

Abstract

The condition of couplings needs to be monitored to predict when they need to be serviced or replaced. Various studies have shown the applicability of Hall-sensors in measuring the position of rotating shafts. The results of these investigations were applied in this research to create a set up for measuring commonly occurring problems in couplings such as shaft misalignment and backlash due to wear. Over the course of this research, it was observed that Hall-sensors were a reliable tool to obtain continuous and contactless measurement of factors related to the condition of the coupling. The application of Hall-sensors aided in the development of a low-cost coupling condition monitoring system. However, the system was sensitive to several external factors which makes retrofitting challenging.

Introduction

Couplings are engineering components that are widely used in power transmission purposes. Like all mechanical components, couplings are subject to wear upon use. The most common causes of coupling wear include lack of lubrication, worn out fasteners, and shaft misalignment [1]. However, other factors like cracks in the shafts or the coupling can affect coupling condition. Coupling breakdowns can be expensive which highlights the importance of monitoring the aforementioned factors. Therefore, the aim of this study was to develop a coupling condition monitoring system for predictive maintenance, focusing mainly on measuring coupling backlash and radial shaft misalignment with the help of Hall-sensors.

Jezny et al. have proven the capability of Hall-sensors in position measurement using the output analogue voltage [2]. The application of linear Hall-sensors and permanent magnets in measuring angular position was discussed by Lee et al [3]. The investigation stated that these sensors can be used to obtain continuous and reliable results without contact with rotating elements. Several other studies have also proven the capability of using Hall-sensors in orientation [4], position [5, 6], and angular measurements [7]. Hence the suitability of Hall-sensors was studied for a retrofittable, low-cost and simple condition monitoring system for couplings.

Background theory

Generally, there are three types of shaft misalignment: radial, axial, and angular [8]. Radial misalignment of shafts can be explained by the combination of vertical and horizontal misalignments. This is illustrated in Fig. 1 below, where, initially, there is vertical misalignment and after a rotation of 90-degrees, there is horizontal misalignment (from the center point of the coupling) of the magnet represented by the black circle.

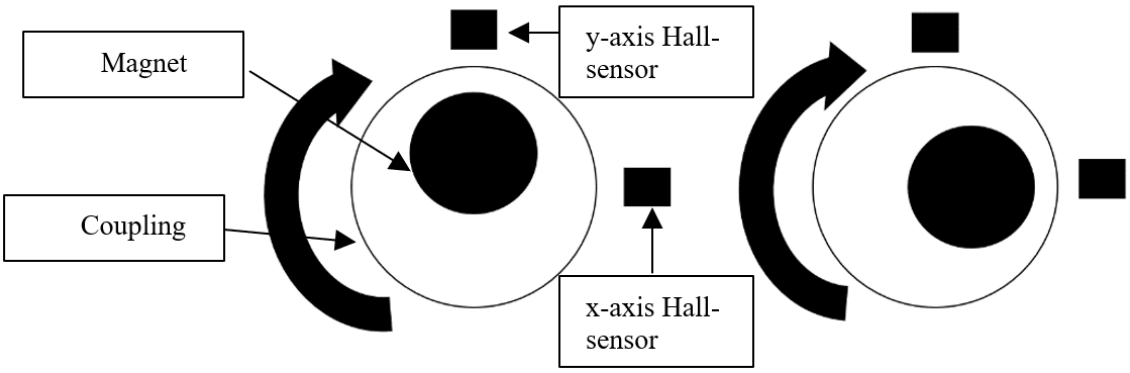

Figure 1. Radial shaft misalignment.

This would cause a scenario where the shaft (and thus the magnet) travels closer to the Hall-sensors on the radially misaligned side. Thus, the Hall-sensor output voltages measured on the radially misaligned side would have greater maximum values than the output voltages measured on the other side of the coupling, which is assumed to be perfectly centered. However, only x-voltage maximum differences were considered in this study. Nevertheless, using both x- and y-voltages for radial misalignment measurement would provide more accurate results.

Axial misalignment occurs when the two sides of the coupling are placed either too far apart or too close to each other. Axial misalignment can cause wear, flexibility issues, and damage in the spider (elastomer) element between the coupling frames. On the other hand, angular misalignment occurs when the centerlines of the two shafts are at an angle to each other. However, these two previously mentioned misalignments are not in the scope of this study.

Coupling backlash can be explained by one side of the coupling being able to rotate with respect to the other side. If once again a magnet is placed on each shaft and the shaft is rotated, backlash could be observed as a phase shift of the sinusoidal voltage signals. This is illustrated in Fig. 2 below, where the complete amount of backlash is obtained by rotating the shafts in both the clockwise and anti-clockwise directions. The phase shift between these two sinusoidal output signals is the backlash of the coupling.

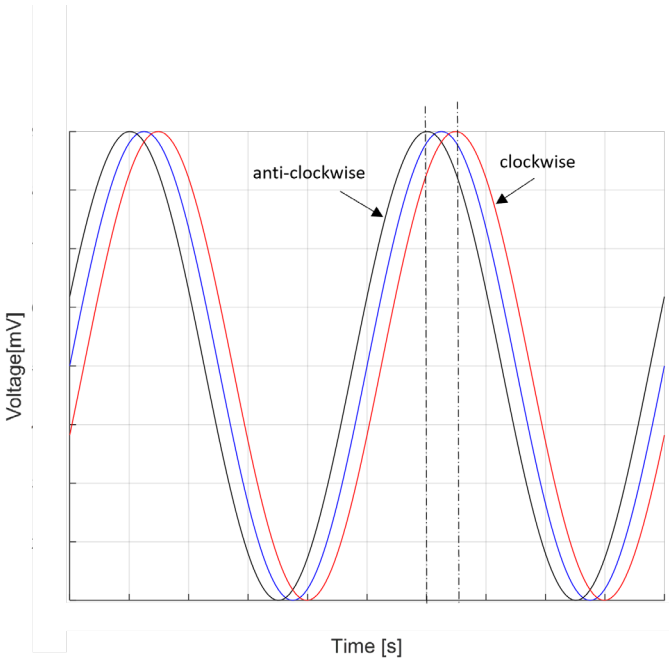

Figure 2. Coupling backlash represented by the phase shift of the output signals.

Methods

System description. The goal of monitoring the state of the couplings was achieved by developing a test rig (Fig. 3) consisting of coupled rotating shafts. Hall-sensors could obtain readings due to the fluctuations in the magnetic fields of the diametrically polarized ring magnets mounted on the shaft and rotating with it.

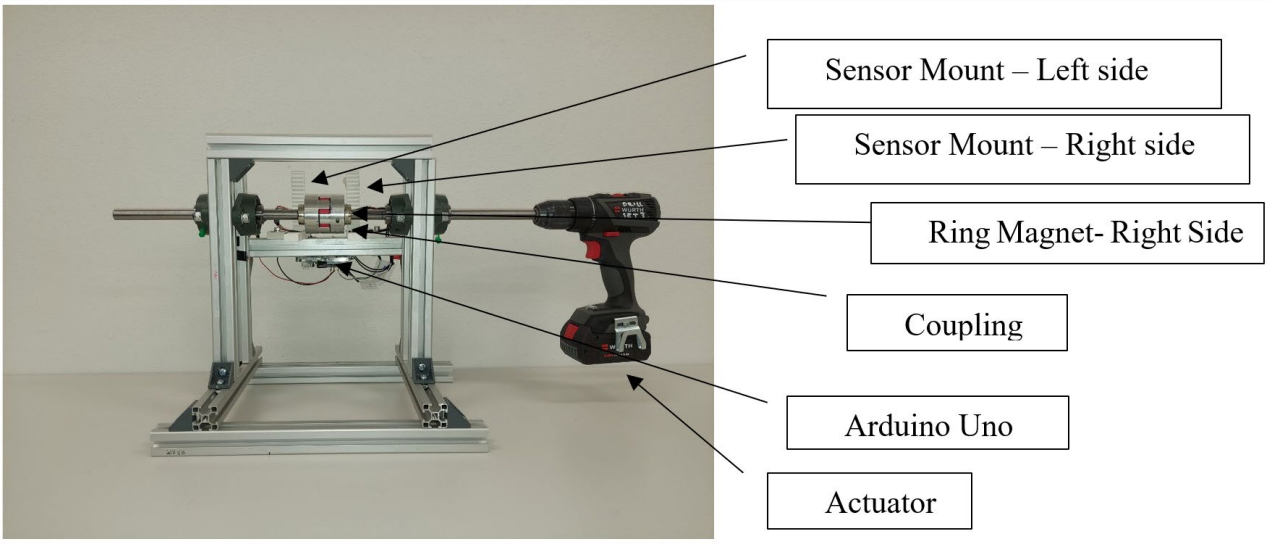

Figure 3. The initial test setup.

The testbed consisted of a stable frame in which the shafts, permanent magnets, mounts for Hall-sensors, coupling, and bearings could be mounted and have their positions adjusted. A flexible jaw coupling with a clamping hub was used, as they are commonly utilized. The Hall-sensors used were Texas Instruments DRV5055-Q1 A4. The mounts for the Hall-sensors were 3D printed and an Arduino Uno was used to read the sensor outputs. One of the 3D printed Hall-sensor mounts was later replaced with a fixture to accommodate a micrometre, on which one of the Hall-sensors was mounted. This setup was used to get a reliable distance to the magnet, as obtaining the calibration curve needed a more precise method of positioning the Hall-sensor. However, the initial setup shown in Fig. 3 was used for the measurement of coupling backlash.

Testing procedures. The testing procedures started with deriving the Hall-sensor calibration curve of distance from the magnet versus the maximum voltage output. The distance was varied using the micrometre. The calibration curve was later used as a predictive model for shaft position, and thus misalignment. After obtaining the calibration curve, both sides of the coupling were positioned so that the Hall-sensors were 6 mm away from the magnets using a reference piece between the sensor and the magnet. Next, misalignment was induced on the right side by changing the distance between the Hall-sensor and the magnet. Radial misalignment can be induced in this way since only the maximum voltages were considered. Moving the sensor closer to the magnet has the same effect on maximum voltages as if the shaft itself was radially misaligned and thus comes closer to the magnet during rotation. This is illustrated in Fig. 4.

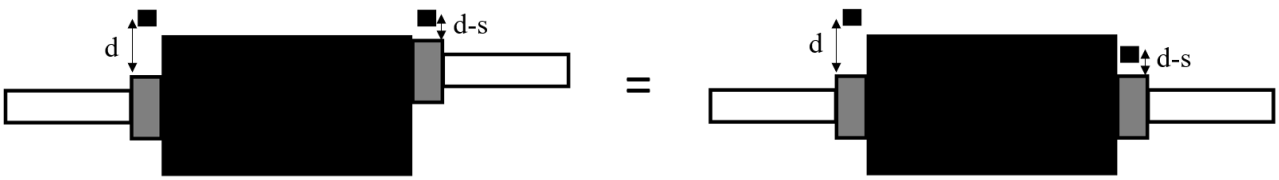

Figure 4. Moving the Hall-sensor closer on one side has the same effect as radial misalignment.

The measurements of coupling backlash were done by 3D printing several deficient coupling spiders and fitting them to the original coupling, thus simulating spider wear and inducing coupling backlash. During the measurements a load was added, and the shaft was rotated in both clockwise and anti-clockwise directions to obtain the amount of coupling backlash.

Results

The calibration curve. The calibration curve was obtained by placing the Hall-sensor at specific distances from the magnet. The curve is shown in Fig. 5.

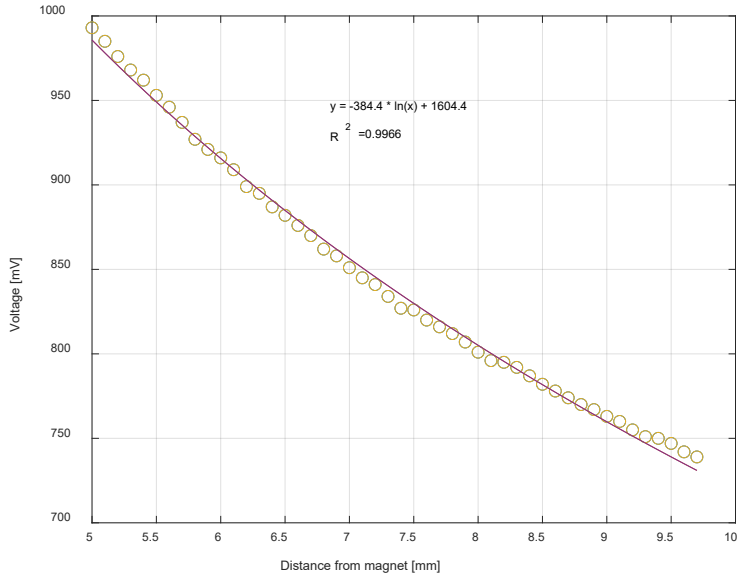

Figure 5. Calibration curve for the Hall-sensors.

Results for radial misalignment and coupling backlash. Fig. 6 below presents the results for both the radial misalignment estimation and backlash.

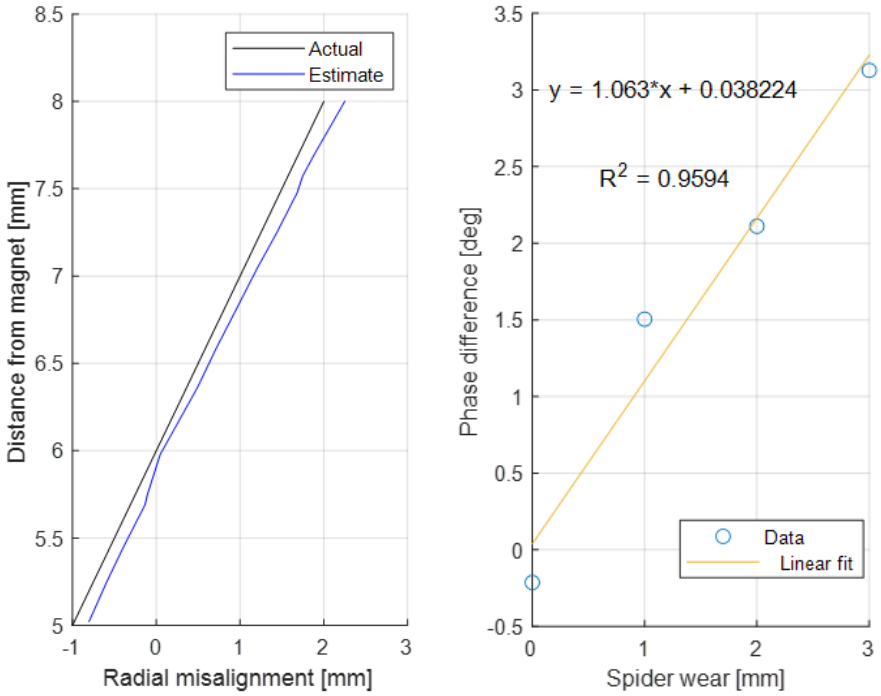

Figure 6. Data and fits for radial misalignment and coupling backlash.

Analysis and reliability of results

The analysis of the results suggests that the distance from the magnet and measured maximum voltage have a logarithmic relationship represented by the calibration curve (Fig. 5). It can also be noted that the calibration curve provides a very good estimation model for the distance between the Hall-sensor and the magnet. This can in turn be used for estimating the misalignment of shafts by comparing the estimated positions of each side. The accuracy of the prediction model can be seen in Fig. 6, on the left-hand side, where the actual positions and misalignments are compared to the estimated ones. The estimated-curve is very close to the actual-curve. In fact, the average error of the estimated position is only 0.13 %. Misalignments could also be predicted very accurately, and have an average error of 0.17 mm.

Many factors induced errors in the measurements. These errors included runouts of the magnets, which were measured to be 0.33 mm on the left side and 0.38 mm on the right side, which is a significant error source. Furthermore, there might have been some small errors in the calibration of the system before measuring, causing the calibration curve to be slightly off. During measurements, it was noted that the measurement equipment was very sensitive to vibrations and the flatness of the surface on which the device was set upon. Hence, these could have caused errors in the measurements.

The results above would also suggest that the relationship between spider wear and the phase difference angle has a linear relationship. It can be seen in the right side of Fig. 7 that the R^2 value is close to one, which means that the fit is good.

It can thus be deduced that Hall-sensors can be used to measure radial misalignment and coupling backlash very accurately. This result implies that Hall-sensors can be used as a tool for measuring factors related to coupling wear and thus enables the maintenance of the coupling before it or the equipment attached to it is damaged. However, it is important to note that the calibration curves and phase shift measurements should be done for each different magnet, coupling, and each Hall-sensor, since there might be differences in these. For example, a larger coupling could tolerate higher amounts of spider wear, since the phase shift angle is directly related to the diameter of the coupling.

Discussion

The results presented in this study suggest that Hall-sensors can be used in measuring coupling backlash and radial misalignment. These are two factors that directly affect the condition of the coupling. Therefore, it could be stated that Hall-sensors can be used in the estimation of coupling condition. However, it is important to note that many other factors affect coupling condition, including other types of misalignments such as axial and angular. Furthermore, cracks and lack of lubrication also have an impact on the condition of the coupling. All these factors, and possibly others as well, would need to be considered when estimating the real condition of the coupling. Some of these factors are easier to estimate compared to others, for example, coupling manufacturers have set tolerances for different types of misalignments for each specific coupling.

Some further applications for the system could include aligning shafts for which couplings are yet to be installed. Additionally, the condition of other components such as bearings, or shafts could be investigated. Shaft misalignments cause additional loads on the shaft bearings and could cause them to wear out sooner, so a quick measurement of the shaft alignment can provide valuable information about bearings and their condition.

The aim of this study was also to make the system low-cost and retrofittable. Although a low-cost solution was found, since Hall-sensors and magnets are relatively cheap, the solution was not easily retrofittable. The system was very sensitive to outside factors such as vibrations and slightly tilted surfaces. Furthermore, the runouts of the magnets also affected the results. Therefore, the sensitivity of the system could create some difficulties for implementing the system in practice, since the operating environments of couplings can be very dirty, include shafts that rotate very quickly and induce vibrations. However, the full effects of these factors cannot be stated as they were not in the scope of this study and should be researched further.

References

[1] K. W. Wattner, "High speed coupling failure analysis," in *Proceedings of the 4th Turbomachinery Symposium*, Texas A&M University. Gas Turbine Laboratories, 1975.

[2] J. Jezný, "Position Measurement with Hall Effect Sensors," American Journal of Mechanical Engineering, 03 10 2013. [Online]. Available: http://pubs.sciepub.com/ajme/1/7/16/index.html.

[3] Y. Y. Lee, R. Wu and S. T. Xu, "Applications of linear Hall-effect sensors on angular measurement," in *2011 IEEE International Conference on Control Applications (CCA)*, 2011.

[4] L. Yan, B. Zhu, Z. Jiao, C.-Y. Chen and I.-M. Chen, "An Orientation Measurement Method Based on Hall-effect sensors for permanent magnet spherical actuators with 3D magnet array," *Scientific Reports ,* vol. 4, no. 6756, 2014.

[5] W. T. Wu, "Rotational position sensor with a Hall effect device and a shaped magnet". USA Patent US5159268A, 21 February 1991.

[6] Z. Q. Zhu, Y. F. Shi and D. Howe, "Rotor position sensing in brushless ac motors with self-shielding magnets," *American Institute of Physics.,* (2006).

[7] J. Kim, S. Choi, K. Cho and K. Nam, "Position Estimation Using Linear Hall Sensors," *IEEE,* 2016.

[8] "The Fundamentals of Coupling Misalignment," Engineering Update, 16 8 2018. [Online]. Available: https://engineering-update.co.uk/2018/08/16/the-fundamentals-of-coupling-misalignment/. [Accessed 7 3 2022].

Test Equipment for Curved Aerostatic Bearing

Jaakko Majuri[1, a], Priya Singh[1, b], Severi Tikka[1, c], and Mikael Saksi[1, d] Petri Kuosmanen[1, e] and Panu Kiviluoma[1, f]

[1] Department of Mechanical Engineering, Aalto University, Finland

[a]jaakko.majuri@aalto.fi, [b]priya.singh@aalto.fi, [c]severi.tikka@aalto.fi, [d]mikael.saksi@aalto.fi, [e]petri.kuosmanen@aalto.fi, [f]panu.kiviluoma@aalto.fi

Keywords: static load, simulation, test equipment, aerostatic bearing, paper machines

Abstract

Reducing friction between two moving bodies helps in reducing the energy loss of the whole system. Aerostatic bearings are known for producing low friction between their surface and the counter surface. However, the behaviour and performance of curved aerostatic bearings are difficult to predict. In this research, a test set-up was designed to study the behavior of curved aerostatic bearings under 25 kN of static load. The test set-up consists of a curved aerostatic bearing, a mounting frame, and a loading device to apply the load onto the aerostatic bearing. Simulations of all these parts were carried out with Creo Simulate. Displacement analysis showed frame and bearing deflection of 0.13 mm and 0.07 mm respectively, confirming that the set-up can be used to study the behavior of a curved air bearing under 25 kN load.

Introduction

Around 15…25 % of the energy consumption in the paper machine industry originates from overcoming friction [3]. There have been studies which indicate aerostatic bearings to reduce the friction. Thus, it would be worthwhile investigating whether aerostatic bearings (Fig. 1) could help to reduce some of this energy loss. Aerostatic bearings use an external pressure supply to create an air film in the range of 5…15 micrometers. This thin air film acts as a lubricant between two surfaces in relative motion [1]. As aerostatic bearings eliminate the contact between surfaces, they have better performance than conventional bearings in high-speed applications, whilst still being able to maintain high-rotational precision [4]. Conventional mechanical bearings are more subject to rapid wear and excessive heat generation in these applications, which can lead to premature failure [5].

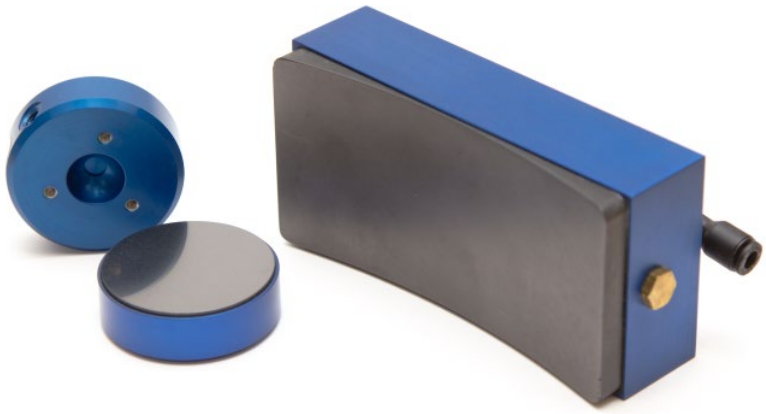

Figure 1. Example of flat and curved aerostatic bearings [1].

Flat-surfaced aerostatic bearings have been investigated with promising load-carrying capacity of up to 18.4 kN. Best performance index load capacity is about 12 kN with bearing dimensions of 270 mm x 110 mm. Scaled up to paper machine roll bearing application, this capacity would mean an estimated line load capacity of 86 kN/m for zone-controlled, and 229 kN/m floating deflection compensated rolls [1]. However, to effectively test a curved aerostatic bearing for industrial application, it is necessary to create a test set-up on a test roll, representing more closely paper machine applications. The goal of this project is to create a test device to investigate the load-carrying capacity of the aerostatic bearing on a curved surface. A simplified image of the loading scenario is shown in Fig. 2 and the test set-up must fulfil the following requirements:

1. Control position of the bearing.
2. Aerostatic bearings are interchangeable.
3. 25 kN load carrying capacity.
4. Measure force applied on the aerostatic bearing.
5. Overall system deflection less than ±1 mm.

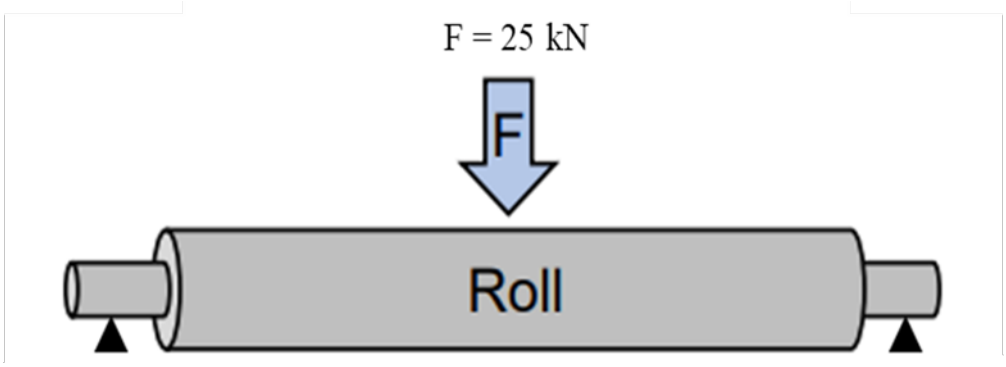

Figure 2. Simplified visualization of the loading scenario. Roll bearings act as pin supports.

Methods

The test equipment consists of three distinct sub-assemblies: a curved aerostatic bearing, a loading device, and a frame (Fig. 3). The aerostatic bearing will be loaded against the test roll from above due to roll mounting not withstanding upward forces. The aerostatic bearing is attached to the loading device mounted to frame with reactive rods. Ball screw with a geared servo motor is used to generate loading force.

Curved Aerostatic Bearing. Section view of the curved aerostatic bearing designed for this experiment is shown in Fig. 4 . A graphite ring is set in an aluminium ring, which is referred to as gum. Between the gum and the bearing frame is a silicon tube. Silicon tube is supplied with air to form a preload. Graphite ring is supplied with air via two channels. Air flows through the graphite against surface the bearing is mounted on. This air forms a seal, which isolates the chamber in the middle. As this chamber is pressurized, heavy loads can be carried. The silicon tube and the spring plates allow the bearing seal to adjust against surface irregularities and misalignments. Aerostatic sealing can deflect up to 2 mm, hence the system has tolerance for adjustment of ±1 mm. A flat aerostatic bearing design offered only 0.26 Nm of friction moment under axial misalignment of 0.175° [1]. This means flat bearing end deflection of ±0.41 mm.

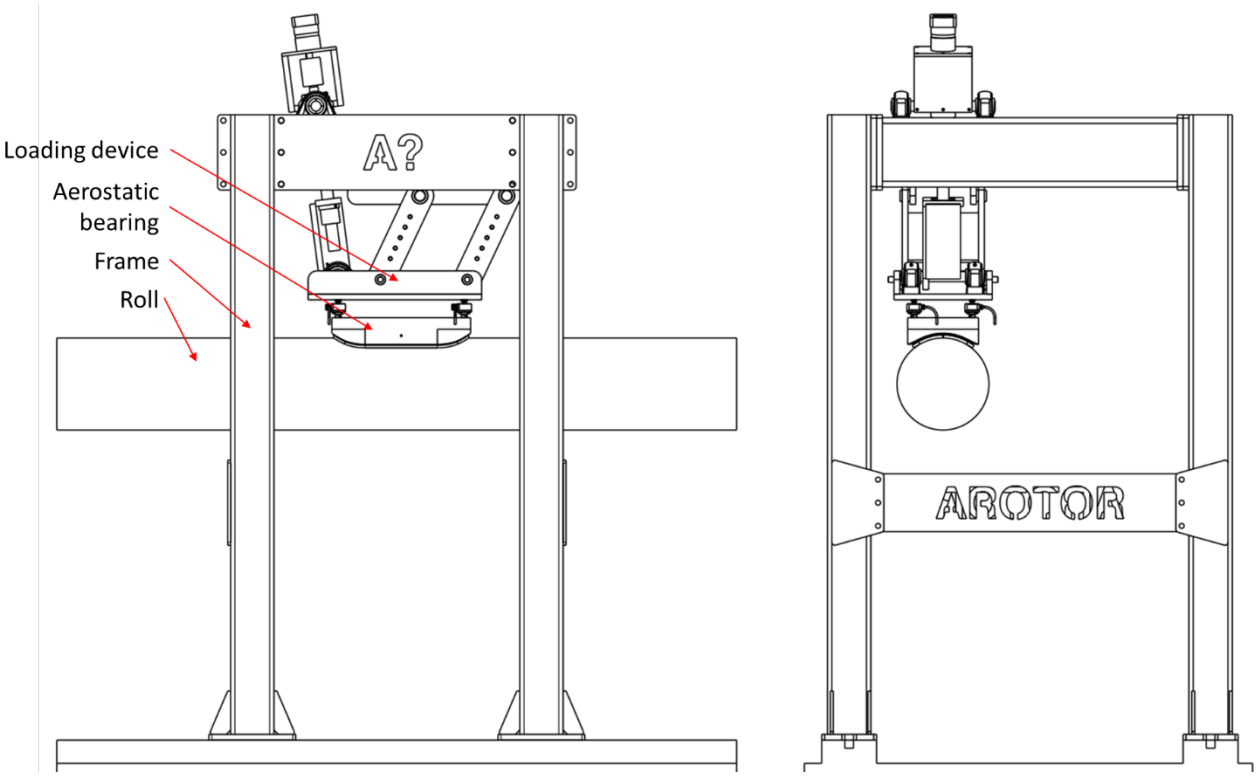

Figure 3. Sub-assemblies of the test equipment.

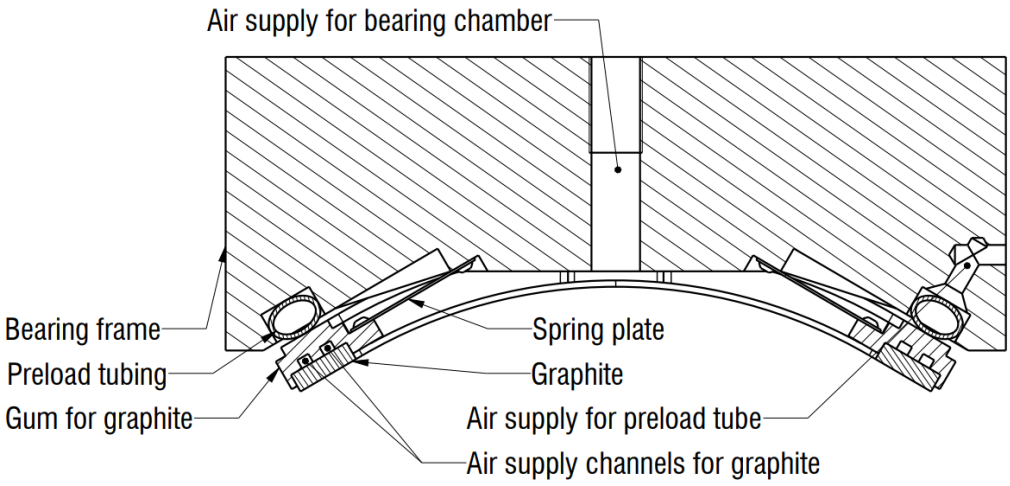

Figure 4. Section view of curved aerostatic bearing.

Loading device. The requirements for the loading device are the following:

1. 25 kN load generation.
2. Precise position control.
3. Measurement of applied force.
4. Overall system deflection less than ±1 mm

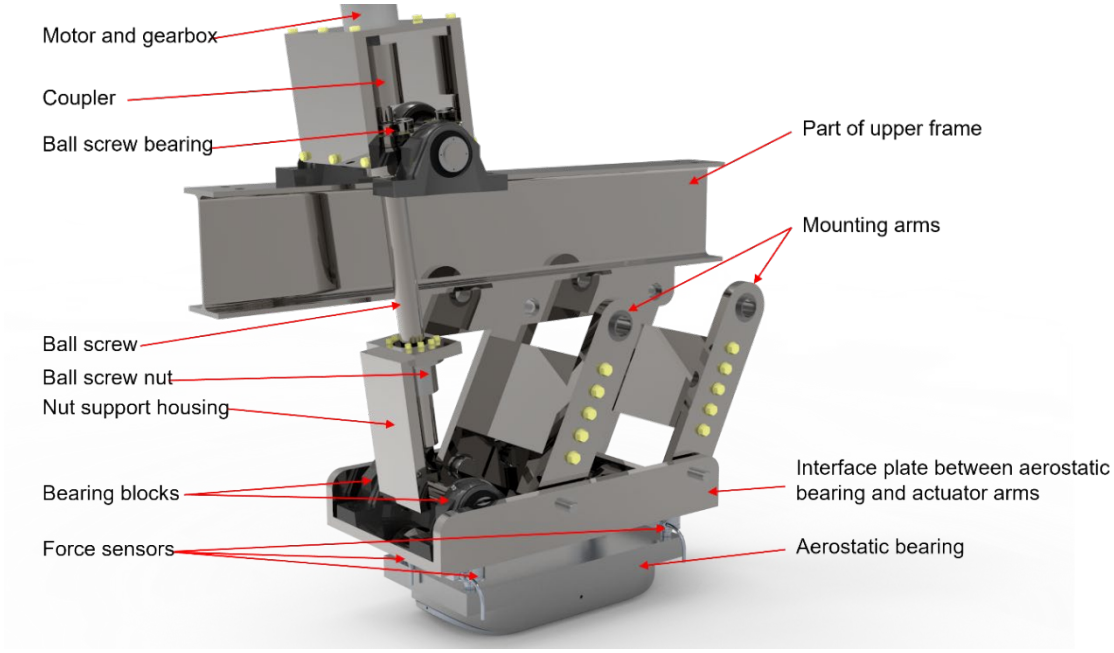

Figure 5. Components of loading device.

As shown in Fig. 5 the loading device consists of two mounting arms, a linear actuator, force sensors, and a central plate. The linear actuator system consists of a 750 W servomotor with a 25:1 planetary gear and a brake to ensure no unwanted movement occurs. The servo motor drives a rotating shaft with a heavy-duty ball screw. As a result, the ball screw exerts a force on a bracket that is connected to the interface plate. The central plate is connected to the aerostatic bearing with force sensors in between them. The ball screw's upper bracket is placed in a position that would maximize the downward load without inhibiting the movement of the plate. The ball screw enables the loading system to accurately control the force applied to the roll. The mounting arms keep the plate horizontal and allow it to move in a consistent arc enabling upward motion as well.

Frame. Fig. 3 shows the frame design with an aerostatic bearing and loading device. The frame was designed to be as rigid as feasible, as it reduces error sources for future studies of the bearing. Frame has multiple bolted interfaces for easy assembly and disassembly. The interfaces are designed in such a way that the horizontal and vertical positioning of the system is adjustable, to allow precise alignment of the aerostatic bearing. Fig. 6 shows the complete test set-up with roll on its mounting, driving motor on the right and error input motor on the left.

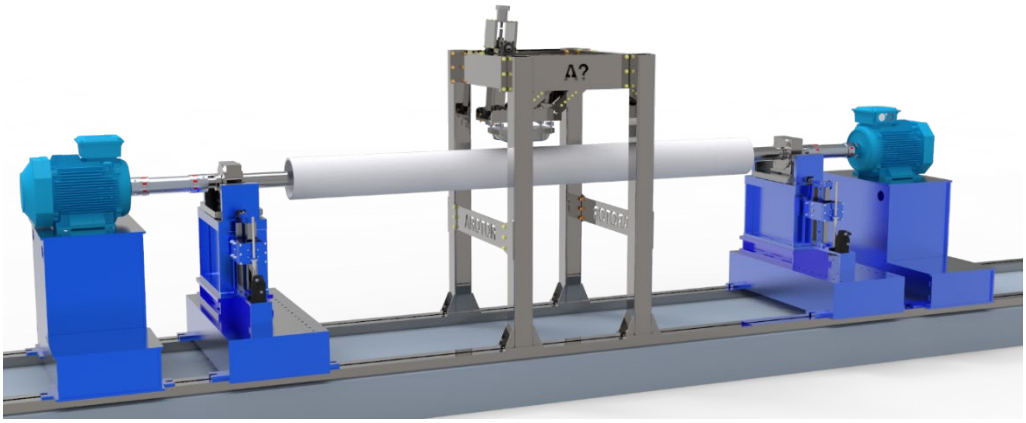

Figure 6. Complete test set-up.

Results

By using FEM simulation, deflection analyses were performed on the frame, loading device, and the aerostatic bearing. For frame and loading device, maximum deflection was studied. For aerostatic bearing gum, deflection analysis was used to find correct spring plate thicknesses. Correct spring plates ensure that, under load, gum deflects simultaneously all around it to ensure good chamber seal. If spring plates are poorly selected, some part of the gum may deflect more than others, creating a leak to air seal under graphite. For simulations, Creo Simulate was used. Fig. 7 and Fig. 8 show the results with maximum displacements of 0.07 mm and 0.13 mm for the loading device and the frame respectively. Both the systems were simulated with a load of 25 kN. Figure 9 shows the results for bearing gum with 0.75 mm spring palates in the middle, at the ends plate thickness of 0.25 mm and rest of the plates have a thickness of 0.5 mm.

In the loading system, the maximum deflection was apparent on the opposite side of the ball screw interface (right side of Fig. 8). This is the result of mounting arms having free moving joints, that do not carry load as much as the ball screw, hence the aerostatic bearing must carry more load on the opposite side of ball screw and thus it deflects more. In the simulation, it was assumed that the frame, to which the loading device attaches to, does not deflect. On the other hand, the maximum displacements in the top section of the frame occurred in the ball screw bearing and motor housing, as can be seen in Fig. 7. This is because the motor housing is the first point of contact for the equal and opposite force generated by the ball screw mechanism.

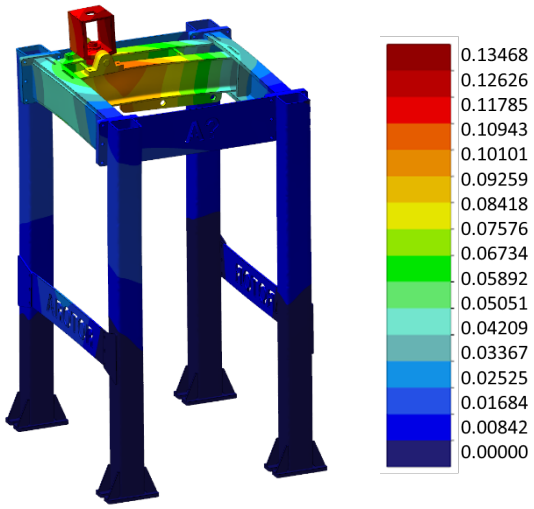

Figure 7. Displacement of frame under 25 kN load. Scale unit: mm

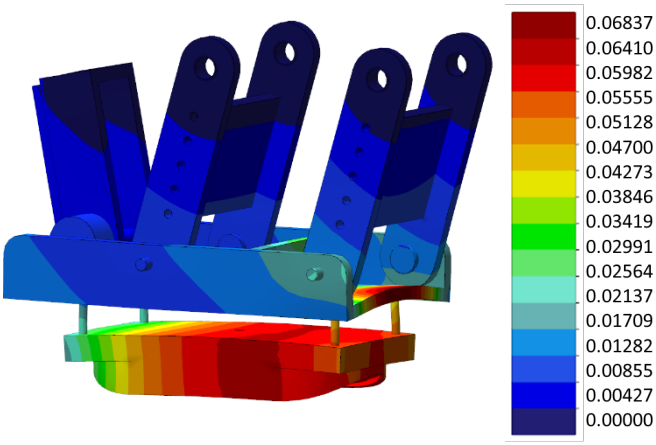

Figure 8. Displacement of loading device under 25 kN load. Scale unit: mm

In simulation of the bearing gum, it was assumed that preload and bearing load cancel each other almost completely, with minor force acting on the gum from preload side. In addition, the simulation accounted for the pressure acting on the gum from inside the chamber. By using the springs mentioned earlier, gum deflected roughly equally at every point, confirming the choice of spring plate thicknesses.

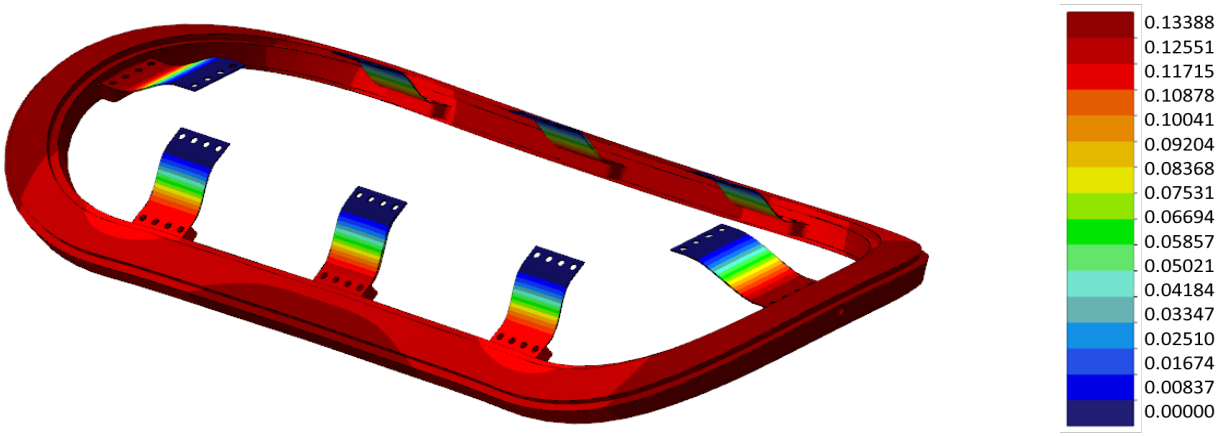

Figure 9. Displacement of bearing gum with suitable spring thicknesses. Scale unit: mm.

Discussion

The results show that frame will have some deflection, though it is designed to be excessively rigid considering the forces applied. This deflection is smaller than maximum allowable deflection defined by the bearing, but its effect on bearing behaviour under dynamic loading situations remains unknown.

Largest source of uncertainty in frame simulation is the force transferred to the frame by mounting arms of the loading device. Therefore, simulations were carried out conservatively assuming most of the loading force is carried by the ball screw. Such assumption was made since mounting arms connect to frame with pin type joints and presumably don't carry much load. This in turn increases frame deflection, as ball screw mount deflects the most as seen in Fig. 7. As exact forces in ball screw and mounting arms are unknown, it is not possible to determine lateral forces applied to frame.

Mounting arms create the same uncertainty to loading device as well, but more importantly, force sensor rigidity is not known. In the simulations, placeholders were used, but since they do not compare to actual sensors, they create a source of error. In addition, loading device simulation is performed assuming no frame deflection and loading force applied to the aerostatic bearing. This approach was chosen, since the force acting on the bearing is known, but force carried by the mounting arms is not. In addition, the roll, against which bearing is loaded, will deflect, and therefore not give accurate result.

References

[1] Miettinen, M. (2021) *Aerostatic seal for pressure chamber*. Master's thesis, Aalto University

[2] Hübner, M. et al. (2021) *Behaviour of porous aerostatic bearings with various restrictor permeabilities.* Proceedings of the 21st International Conference of the European Society for Precision Engineering and Nanotechnology, EUSPEN 2021, ISBN: 9780995775190

[3] Voith Paper GmbH. (2006) *Deflection compensating rolls by voith – reliable technology for a market orientated quality of your paper and board grades*", Krefeld/Manchester/Springfield, Datasheet.

[4] Celeramotion (2022) *What is an air bearing*. [referenced 5.4.2022] Available at: https://www.celeramotion.com/westwind/support/technical-papers/what-is-an-air-bearing/

[5] Machine designs (2016) *Advantages of air bearings.* [referenced 5.4.2022] Available at: https://www.machinedesign.com/mechanical-motion-systems/bearings/article/21831998/advantages-of-air-bearings

Effect of Reused Exhaust Air in Pneumatic System

Lorenzo Ceppari[2,a], Kim Hirvonen[1,b], Anna-Kaisa Korhonen[1,c], Oliver Olin[1,d],Jyrki Kajaste[1,e], Panu Kiviluoma[1,f] and Petri Kuosmanen[1,g].

[1] Department of Mechanical Engineering, Aalto University, Finland

[2] Department of Mechanical Engineering, Politecnico Di Torino, Italy

[a]s290655@studenti.polito.it, [b]kim.hirvonen@aalto.fi, [c]anna-kaisa.korhonen@aalto.fi, [d]oliver.olin@aalto.fi, [e]jyrki.kajaste@aalto.fi, [f]panu.kiviluoma@aalto.fi, [g]petri.kuosmanen@aalto.fi

Keywords: energy saving, pneumatic efficiency, compressed air reuse.

Abstract

Pneumatic systems are widely spread in industry. One major downside of these systems is their low efficiency. In traditional systems the exhaust air from the actuators is released into the atmosphere, which results in a waste of energy. The goal of this study was to analyse the effect of a pneumatic energy saving unit that is recirculating exhaust air in pneumatic system. Results showed a clear improvement in energy efficiency of the system when this unit was applied.

Introduction

Pneumatic actuators are widely used components globally in industry. It has been estimated that around 10% of the total industrial electricity power consumption in the EU can be attributed to compressed air systems. [1] In the U.S.A. pneumatic equipment consumes roughly 530 PJ of energy annually, which correlates to $10 billion worth of energy per year. An increase of 15% to 30% in energy efficiency would correspond to $1.5 billion annual savings. In most applications the exhaust air from actuators is released into the atmosphere resulting in waste of energy. Instead of releasing the exhaust air out of the system, it can be reused. [2]

Various methods for increasing pneumatic energy efficiency have been studied before. Joshua J et al. studied energy conservation in industrial pneumatics by developing a state model for predicting energy savings due to a novel pneumatic strain energy accumulator. The results showed an increase in efficiency. [3] Vladislav Blagojevic et al. improved energy efficiency in the execution part of a pneumatic system with a semi-rotary actuator by adding a bypass valve to the actuator. The study concluded significant savings in air consumption. [4] Furthermore, Blagojevic et al. presented a cylinder control system with a piston rod on one side where energy savings were reached by tuning supply pressures and holding the piston in a certain position [5]. Fan Yang et al. analysed, which factors most affect the efficiency of a pneumatic booster with energy recovery (VBA-R) and concluded that recovery chamber increased the efficiency by 5% to 10% [6]. Takahiro Kanno et al. developed a poppet-type pneumatic servo valve to minimize air leakages, which has a ratio of air leakage to maximum flowrate of 0.37% [7]. Olivier Reinertz et al. developed a method for efficiency improvement of pneumatic boosters based on a mathematical model [8].

The aim of this study was to measure the efficiency increase of a pneumatic system when exhaust air of the actuator is recirculated through pneumatic energy saving unit (PES-unit) back to the system instead of releasing it into the atmosphere.

Methods

A test system (Fig. 1) was built for performing pneumatic efficiency measurements. The PES-unit (B) was installed in the test setup.

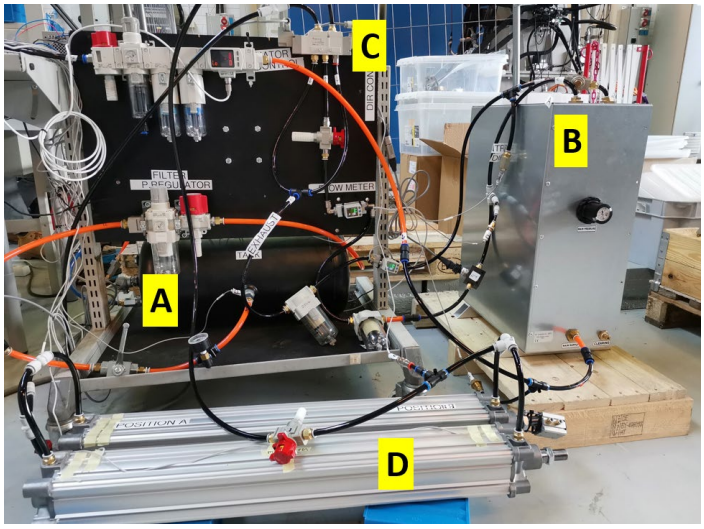

Figure 1. Pneumatic test system. (A: tank, B: PES-unit, C: directional control valve, D: actuator)

Tests were made with two different system set-ups: with and without the PES-unit. Fig.2 presents the schematic of the set up with the PES-unit. The components of the system are numbered and listed in Table 1. In tests without the PES-unit, air supply is directly connected to the directional control valve and the exhaust air is released into the atmosphere through a silencer.

Air tanks (4) are used to storage the air used in the tests. Actuators are operated with a 5/3 directional control valve (7). Since PES-unit causes back pressure to the exhaust side slowing the piston speed, throttle valves (8) are used in tests without PES-unit to adjust pressure and speed to same level, making tests comparable. Pressure, temperature, and flow metering sensors were installed to keep track of the changes in the system.

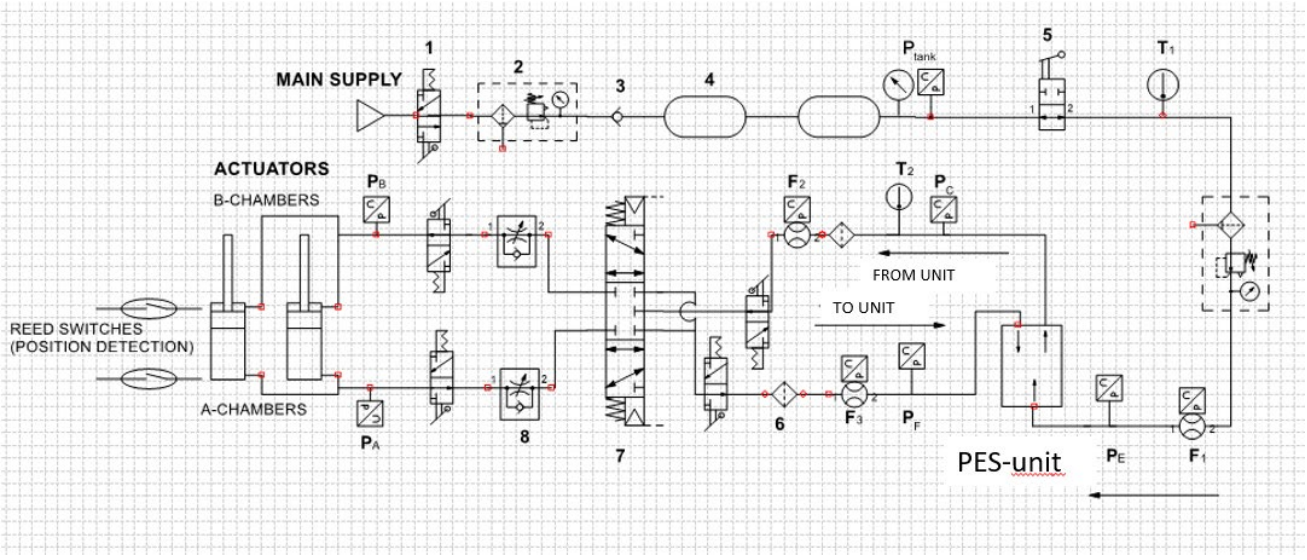

Figure 2. Schematic of the system with the PES-unit

Table 1. Components in the system.

Number/letter	*Component*	*Code/manufacturer*	*Specs*
1	Shut-off valve with exhaust port	EVHS3500-F02-X116	
2	Air maintenance unit	SMC	
3	Check valve	AK2000	
4	Air tank	PREMI	Volume 30 l
5	Stop valve	PN500	
6	Air filter	AFM40-F04-A	
7	5/3 directional control valve	SY9320-5YZ-03F-Q	
8	Speed control valve	AS3002F	
9	Silencer	AN200	
P	Pressure sensor	PSE530-M5	
T	Temperature sensor	20073657	
F	Flow meter	PF3A701H-ES/ PFMC7102-F04-E/ PFMC7501-F04-E	10-1000 l/min range
Actuator (large)	Double acting cylinder	CP96SDB80-700C	Stroke 700 mm Bore 80 mm
Actuator (small)	Double acting cylinder	ECDQ2A 40-25DM	Stroke 25 mm Bore 40 mm

The operation of the PES-unit is explained by referring to a figure in US patent 9,765,786 B2. In Fig. 3 the pressure increasing unit (1) consists of the following components.

2. Means to receive gas from the main source
3. First pipeline
4. Pipeline from the main source
5. Second pipeline
6. Means to receive reduced-pressure gas
7. Pressure intensifier
8. Substitution means
9. Pressure controller
10. First storage tank
11. Third pipeline
12. Second storage tank
13. Fourth pipeline

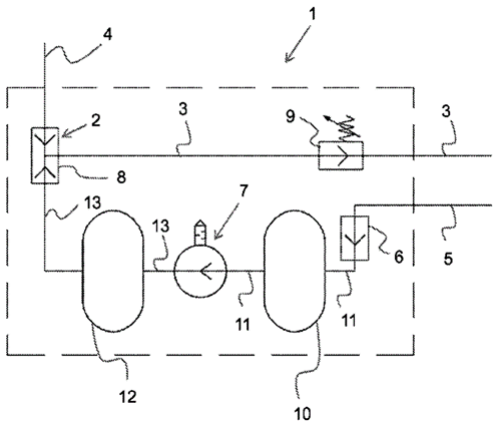

Figure 3. Schematic of the PES-unit. [9]

During a typical use the flow through pressure controller (9) and first pipeline (3) is directed to a directional control valve operating a cylinder actuator. Actuators exhaust air with reduced pressure is fed to the PES-unit through second pipeline (5). In the PES-unit this air flow with reduced pressure is fed back to the system through second pipeline (5). The remaining energy is utilized in the pressure intensifier (7) to produce high pressure air which can then be directed back to the actuator through substitution means (8). This flow is possible when the PES-unit's circuit pressure exceeds the air pressure in pipe (4) which delivers the flow from the main source. With this arrangement the amount of compressed air needed from the main supply is reduced saving energy and diminishing the need for expensive air treatment, because a significant amount of air can be circulated in the system.

Controlling the system was done by using a Beckhoff PLC [C6920-0050]. Sensors and actuators were connected to the I/O terminals, then terminals were connected via Ethernet to the main PLC. At first the directional control valve is in the middle position, i.e., the lock position. When the tank pressure sensor reaches a value of 7 bar, the control algorithm initiates the piston movement by powering the directional control valve. At the beginning of the experiment the piston is always in the

cap end and is moved towards head end. According to the piston's position, the control algorithm actuates the directional control valve to make the piston reach the opposite position. Once the tank pressure sensor reaches a value lower than 4 bar, the directional control valve moves into the centre position and the movement of the pistons is ceased.

Testing of the effect of PES-unit was studied by comparing the number of cycles produced by actuator with certain amount of air, with and without the unit. Flow rates in all PES-unit's ports were monitored. To simulate real-life industrial scenario, tests were done in a pressure range from 7 to 4 bar. To make tests comparable, the same amount of air in both tests was used; 60 l of air at 7 bar was filled to tanks in the beginning of the test. In addition, approx. 0.5 1 of air was estimated to be stored in the components before the tanks. Furthermore, as PES-unit causes back pressure to the exhaust side slowing the piston speed, throttle valves Fig. 2 (8) were used in tests without the unit to adjust pressure and speed to around same level, to make results of the tests comparable.

Test procedure was the following:

1. Closing the stop valve to isolate tanks from other system (Fig. 2, (5)).
2. Filling the tanks up to 7 bar pressure from main supply. Then closing main supply.
3. Opening the stop valve, allowing the air flow further to the system, making the actuator operational. Recording the sensor readings e.g., cycles, flow rates, and pressure values.
4. Operation of the system stops when lower pressure limit (4 bar) is reached.
5. Recorded data is analysed to study the effect of PES-unit in the system.

Force developed in the actuators was obtained using Eq.1. Pressure values were not taken from the piston's chambers but from the piston's supply tube. Air may experience pressure drops when entering the cylinder chambers through narrow ports. The piston and the piston seal friction also affect the actual mechanical force produced by the cylinder. Thus, the force values are an estimation of the real value.

$$F = P_A \cdot A_A - P_B \cdot A_B \quad (1)$$

3 different actuator set-ups were used to analyse the system: in test 1 two large cylinders in parallel were used, in test 2 single large cylinder was used, and in test 3 single small cylinder was used. The sizes of the actuators are listed in Table 1. Table 2 presents the total amount of full cycles done by the actuator in both test set-ups. The tests were performed on a range from 7 to 4 bars.

Results

Fig 4. presents the flow rate to directional control valve when using two large actuators, both with and without PES-unit. Air flow rate from supply is continuous, stable and in same value in both cases. PES-unit provides higher flow rate to the valve, due to exhaust air recirculation.

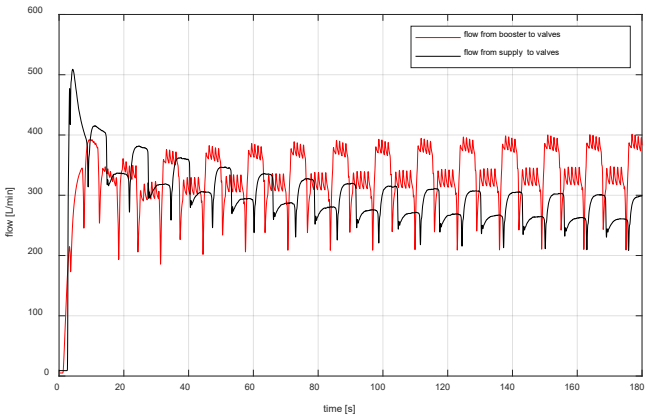

Figure 4. Flow rates to the actuators with constant pressure air supply. (PES-unit=booster)

Table 2 indicates that the PES-unit increases the number of cycles. In test 3, the system does almost double the cycles in a time span which is double of it. This suggest that the pistons' speeds in the two set-ups are very similar.

Table 2. Number of cycles with or without the PES-unit.

	NO PES-UNIT		**WITH PES-UNIT**	
	[number of cycles]	Time [mm:ss]	[number of cycles]	Time [mm:ss]
TEST 1	2	00:26	3	00:38
TEST 2	4	00:30	6	00:39
TEST 3	120	01:05	219	02:07

Fig. 5-8 present data from tests with two parallel large cylinders. In tests without PES-unit, the exhaust flow was throttled to reach approx. the same piston speed and chamber pressure. Magnitude of force is almost same in Fig. 5 and Fig. 6. indicating that the throttling successfully increased the cylinder pressure to the same level. Red dashed line presents cycles done by actuator in Fig.5 and Fig.6. When PES-unit was utilized in the system, an additional cycle was reached. Using the PES-unit, the supply air flow rate is reduced after 20 seconds (Fig.7), while flow rate to the valves is kept constant. When the PES-unit is not used (Fig.8), once the flow rate from the supply reduces, also the flow rate to the valve reduces.

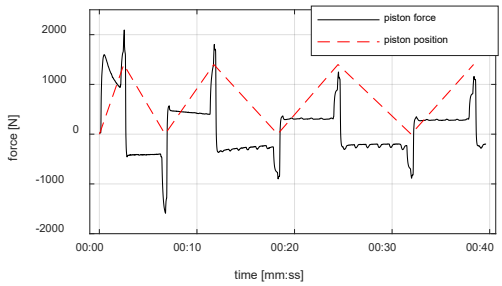

Figure 5. Force plot, with PES-unit.

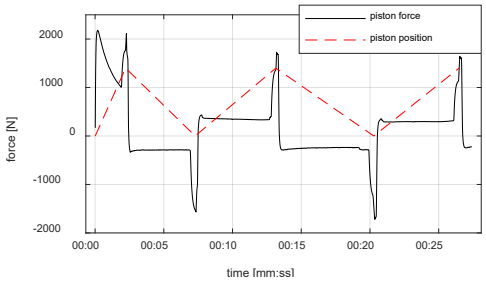

Figure 6. Force plot, without the PES-unit

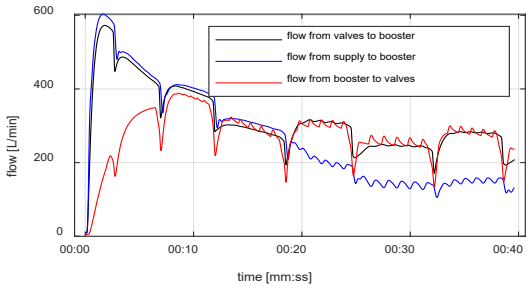

Figure 7. Flow rates with PES-unit(booster) in standard conditions (20°C and 101.3 kPa).

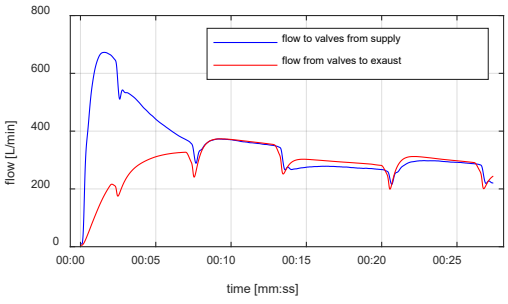

Figure 8. Flow rates without PES-unit in standard conditions (20°C and 101.3 kPa).

Discussion

In tests without PES-unit exhaust air was throttled which is a dissipative way to control a system. When comparing results this should be taken in consideration. To fully understand the advantages of PES-unit used in air recirculation, a rigorous mathematical model to estimate energy efficiency gain should be developed. Quick exhaust valves could have been used in test system by installing them in ports of actuator and connecting then directly to PES-unit or atmosphere to avoid pressure losses in directional control valve. To determine efficiency of PES-unit more precisely shorter hoses with larger diameter could have been used, and valves in the system could have been larger to minimize pressure losses in the system.

The flow sensors report the values in standard conditions i.e., when the pressure and temperature are equal to 101.3 kPa and 20°C. Cylinders used in tests were the ones readily available with built in-magnet which is needed for determining the piston position in the system. In the future, tests could be performed with different size of cylinders. Also, a more advanced system model would be required to be able to analyse the effect of different system components and parameters on the systems energy balance in detail. There are differences in the performance between all the tests TEST 1, TEST 2, and TEST3. The system contained various additional filtering units and shut-off valves which caused extra pressure losses. Typically, they are not present in industrial systems, but were needed in this test circuit. TEST 3 is closest to typical industrial work cycles. The differences may derive from the pressure levels of the cylinder before a new cycle. Anyway, the differences should be further investigated in the future studies.

Summary

The PES-unit was found to increase the overall performance by increasing the energy efficiency due to less air required from main supply for same amount of work. For example, in test with small cylinders, the PES-unit almost double the number of the cycles. As a conclusion, the pneumatic energy saving unit showed great potential in the tests conducted.

References

[1] Siminiati, D. (2011). Price reduction on compressed air. *Engineering Review, 31*, 63-67.

[2] Love LJ, L. E. (2012). *Estimating the impact (energy, emissions and economics) of the U.S.* Oak Ridge (TN): Oak Ridge National Laboratory.

[3] Joshua J. Cummins, C. J. (2017). Barth Energy conservation in industrial pneumatics: A state model for predicting energetic savings using a novel pneumatic strain energy accumulator. *Applied Energy, 198*, 239-249.

[4] Blagojevic, V. A. (2016). Advantages of restoring energy in the execution part of pneumatic system with semi-rotary actuator. *Thermal Science, 20*, suppl. 5, S1599-S1609.

[5] Vladislav Blagojevic, D. S. (2020). Energy Efficiency of Pneumatic Cylinder Control with Different Levels of Compressed Air Pressure and Clamping Cartridge. *Energies*, 13,3711.

[6] Yang, F. &. (2017). Analysis of the Energy Efficiency of a Pneumatic Booster Regulator with Energy Recovery. Applied sciences. *7*, 816.

[7] Takahiro Kanno, T. H. (2018). Development of a Poppet-Type Pneumatic Servo Valve. *Applied science, 8*, 2094.

[8] Reinertz, O. &. (2019). Efficiency optimized pneumatic booster. Symposium on Fluid Power and Motion Control. *Proceedings of the ASME/BATH 2019 Symposium on Fluid Power and Motion Control* (p. 1675). Longboat Key, FL, USA: ASME.

[9] Korpela, S. (2017). *United states of America Patent No. US 9765786 B2*

Development of Electromagnetic Unlocking on Container Semi-Automatic Twistlocks

Pauli Haimilahti[1,a], Michael Brini[1,b], Niklas Jänkälä[1,c],
Ekaterina Alifanova [1,d], Panu Kiviluoma[1,e] and Petri Kuosmanen[1,f]

[1] Department of Mechanical Engineering, Aalto University, Finland

[a] pauli.haimilahti@aalto.fi, [b] michael.brini@aalto.fi, [c] niklas.jankala@aalto.fi,

[d] ekaterina.alifanova@aalto.fi, [e]panu.kiviluoma@aalto.fi, [f]petri.kuosmanen@aalto.fi

Keywords: cargo, contactless, electromagnet, fast-unlocking, shipping, vessel

Abstract. Semi-automatic twistlocks are devices used to secure containers together in a stack on container ships.They are a mainstay of container shipping because they are inexpensive, safe, and reliable. To unlock one, an operator is needed to manually open the lock, a process which can be slow and dangerous. Ideas for the new design were compiled into four (4) main concepts. After grading concepts through a selection matrix, and consultations with the client, a new concept based on a ratchet and pawl mechanism and designed to be opened by an electromagnet, was down-selected for development and prototyping. The reliability of the mechanism will be tested by putting it under a repeatability test. Using a test setup, comprising a standard cargo container with corner castings welded on, the developed twistlock will be continuously locked and unlocked.

Introduction

Global shipping accounts for 90% of world trade [1]. Ship tonnage is growing steadily to accommodate the increased demand for cargo [2]. Both vessels and ports are pressured to speed up operations, particularly the movement of containers [3, 4].

In transit, containers are secured to each other with twistlocks. Although there are minor differences between products, the concept remains consistent [5]. Twistlocks are placed in the bottom corner castings of a container followed by a crane lowering it on top of another container. The shape of the lock is designed such that it slides into the casting below, and locks automatically.

Semi-automatic twistlocks are a proven technology [6]. It is half-automated, requiring a port worker to manually unlock. This increases time in port, risk of accidents and, therefore, costs [7]. Fully automatic locks were an attempt to solve this, however, they have been involved in a series of container losses [8].

Use of automation in twistlocks [3] has been studied to accelerate harbour operations. The limitation for widespread adoption of this technology is twofold. The first limitation is power. Current vessels are not designed to provide power to individual locks. The second limitation is trust by vessel operators. With millions of euros at stake [9] in a potential loss-at-sea, there is hesitancy among vessel operators to adopt twistlocks presenting radical leaps in technology.

Due to the above considerations, focus was placed on developing an internal mechanism that can be quickly opened, without the use of force from a port operator, and without the need to energize the twistlock.

Development Process

Design began with the creation of a development plan (Fig. 1).

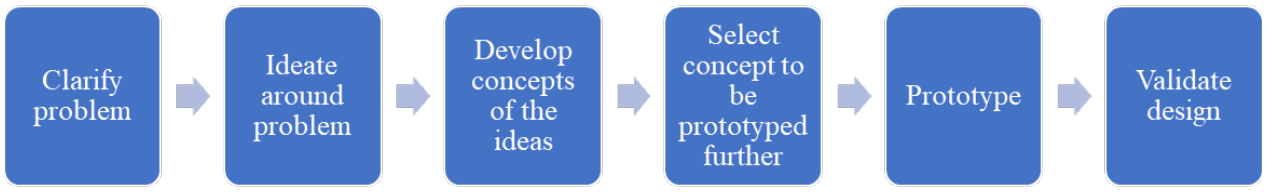

Figure 1. Development plan for the twistlock.

As shown in Fig. 1, the problem was first clarified, and a requirements list was created. The twistlock shall

a) Be capable of operating up to the Safe Working Loads (SWL)
   i. Tension: 250 kN
   ii. Shear: 210 kN
   iii. Compression: 1000 kN
b) Be capable of operating and remaining intact up to 2 x SWL
   i. To be tested and verified by marine classification society
c) Be locked automatically using the weight of the container
d) Be unlocked manually
e) Be capable of being unlocked when located 15 meters above the operator
f) Be capable of being unlocked without the operator exerting force
g) Have a method of re-locking the lock in event of a mistake or emergency

Ideation began around addressing the methods which could be used to unlock the twistlock. After determining which methods would fulfil the design requirements, ideation moved to conceptualizing a mechanism compatible with the unlocking methods. For this, techniques such as *"brainwriting"* – participants, without talking, write their ideas and pass them on for another participant to add to – and *"worst possible idea"* – intentionally seeking the worst ideas – were utilized.

Once there were enough new, feasible concepts, they were presented to the client to determine their suitability for use on a vessel. The remaining concepts (Table 1) were graded on a scale of 1 to 5 according to the grading criteria (Table 2) with the winner moving on for further development and prototyping.

Table 1. Evaluated concepts.

Concept 1	A solenoid lock which contains a rechargeable battery, an RFID tag, a solenoid to operate the shaft of the lock, and a PCB board for automatic operation, as well as a weatherproof housing for the electronics together with the lock itself.
Concept 2	A crew loaded lock, which is charged by the crew who inserts the lock into the lower corner casting of the container. Loading movement makes a spring inside the lock to load the lock, whereas a ratchet system holds the lock closed until a pawl is removed using an electromagnet.
Concept 3	A double cone design, which is opened similarly to the crew loaded lock, but can be charged automatically with a help of another cone around the bottom cone of the lock. Rotation of the additional cone will load another spring, which is strong enough to open the lock when released.
Concept 4	An electromagnetic lock, similar to client's existing model, except the lock is operated using a special operating rod with an electromagnet. The rod will detect an NFC tag in the lock and catch a large steel plate connected to the opening wire of the lock.

Table 2. Grading criteria cover the main requirements weighted according to importance.

Cost	Unlocking Speed	Marine Environment Survivability	Reliability	Feasibility
20%	15%	25%	35%	5%

Table 3. Concept scoring.

	Cost	Unlocking Speed	Marine Survivability	Reliability	Feasibility	TOTAL
	20%	15%	25%	35%	5%	
Concept 1	2	5	4	3	5	3.45
Concept 2	3	5	3	4	4	3.70
Concept 3	2	2	3	2	1	2.05
Concept 4	5	4	1	1	4	2.40

The concept with highest score (Fig. 2) employs a ratchet and pawl mechanism. The twistlock is in a normally unlocked state. When loading a container onto a ship, a port operator inserts the twistlock into the container corner casting and arms the lock by moving the ratchet the full distance until it is locked in place. When in this position, due to the shape of the knob on the bottom twistlock, the weight of the container will push the knob into the corner casting of the container below. A spring will return the knob to the locked position.

When containers are being unloaded from a vessel, the port worker will use the operation rod, a metal pole with an electromagnet at the tip, to release the pawl. The spring force will return the lock to its normally unlocked state and the container can then be removed.

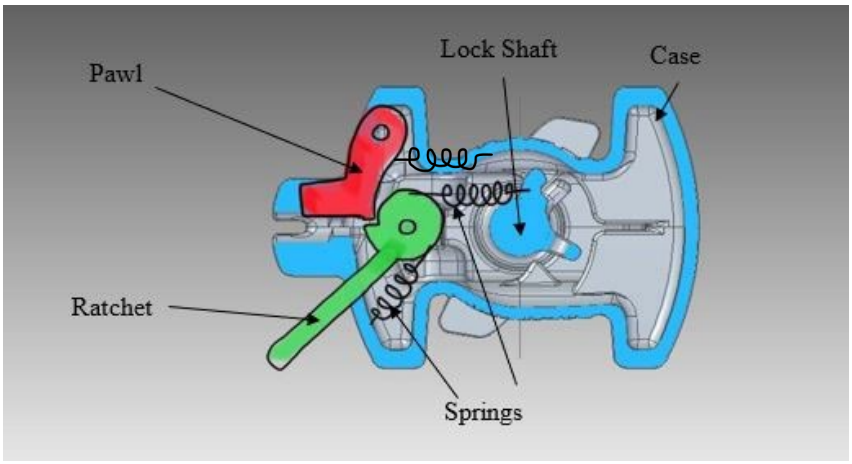

Figure 2. Winning concept selected for prototyping.

The ratchet's handle is prominent for three reasons. First, the handle is easy to grip and provides enough torque for the port worker to arm it. Second, it acts as an indicator as to which state it is currently in. Third, in emergency situations, where the lock has been opened by mistake, it can be relocked by reaching it with the operation rod and pulling the ratchet back to "locked" position.

Results

The force applied by the electromagnet must overcome the spring that biases the pawl towards closed, as well as friction between the pawl and the ratchet. The friction between the pawl and the ratchet can be reduced by modifying the contact angle, enabling to tune the sensitivity of the mechanism.

Proper facilities for testing were not accessible, so proper repeatability and environmental testing could not be completed. Following this, marine classification societies will test it to ensure that it will not break up to two times (2x) the safe working loads in tension, shear, and compression. The design of the prototype version is presented below (Fig. 3).

Fig. 3a presents the 3D model of the lock in its entirety. Fig. 3b presents only the inner mechanism. The design enables fast modifications on the critical dimensions of the real prototype, which explains the number of parts used. The prototype manufactured is shown in Fig. 4 and Fig. 5.

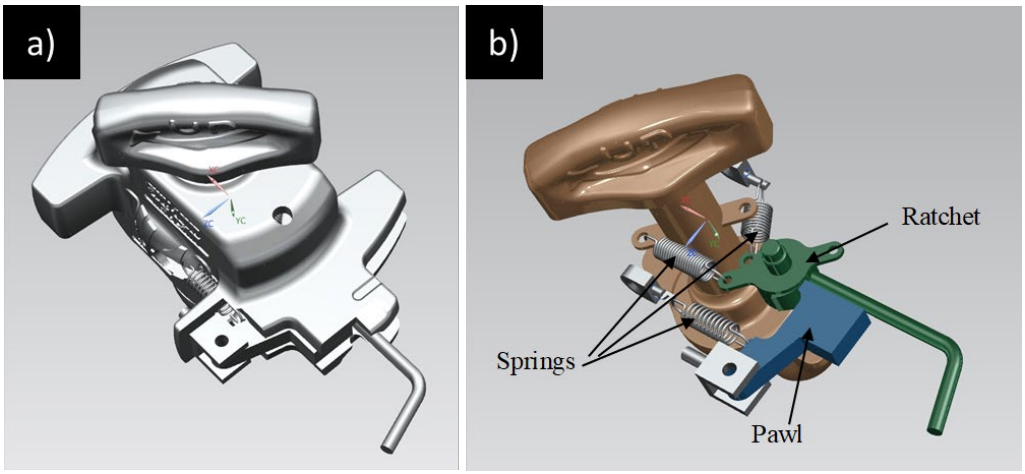

Figure 3. Modeled prototype: a) With case, b) Without case.

Figure 4. Assembled lock without lock shaft in unlocked position.

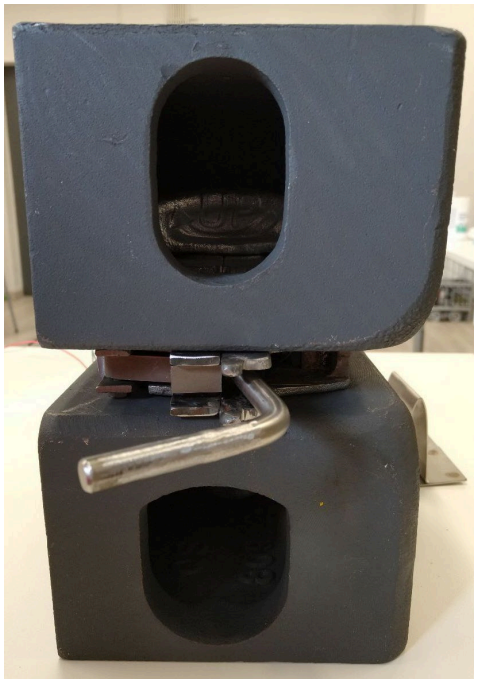

Figure 5. Lock between corner castings. Lock is in unlocked position.

The mechanism of the prototype shown in figures above was tested as it would be used in real situation at harbor. The mechanism worked intentionally: lock can be inserted into the corner casting in a couple of seconds, the design provides an automatic locking on the other corner casting, and the lock can be quickly opened by a strong magnet.

Using an electromagnet enables designing the operating rod to be used differently from the operating rod used in traditional twistlocks, which might help hitting the twistlock faster. Furthermore, it would be possible to get rid of the operating rod and use other type of a device for opening, such as a drone. The design of the operating device is out of the scope of this paper, however, a diagram of the basic principle for an electromagnetic operating rod is presented in Fig. 6.

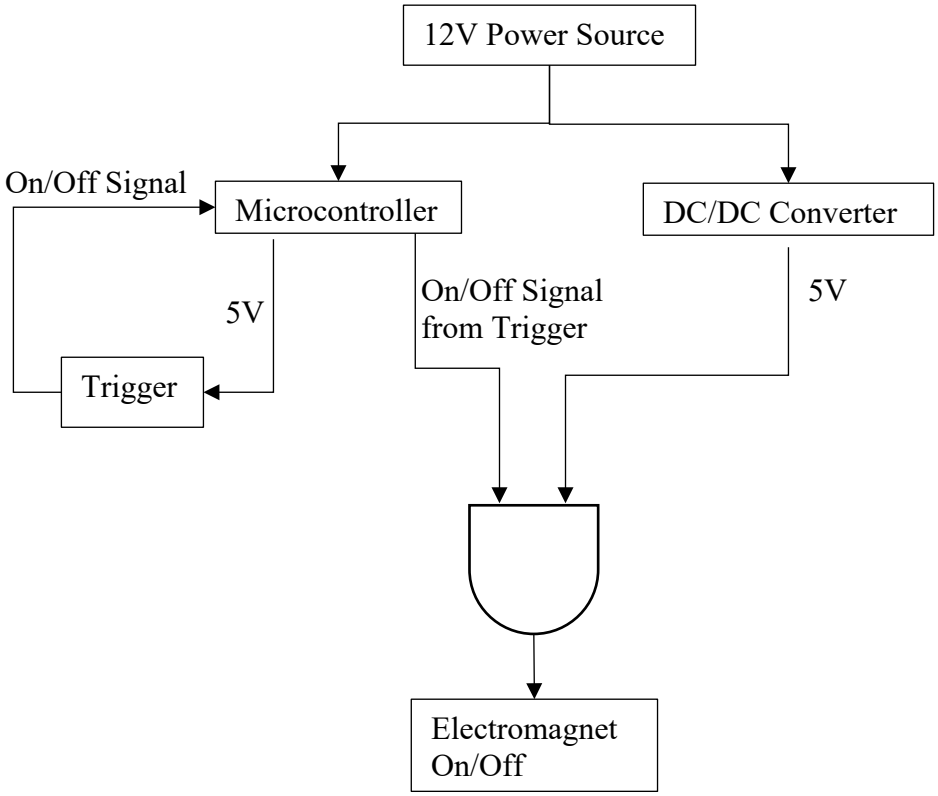

Figure 6. High-level diagram of operating rod for operating the lock.

As shown in the Fig. 6, the trigger and microcontroller are isolated from the higher current the magnet requires, providing safety for the user and protect the microcontroller from damage.

Discussion

The Wavelock improves over the previous generation of semi-automatic twistlocks in two important categories: speed of operation and safety. In normal operation, the switch to a contactless electromagnet allows the user to actuate the lock in less than a second without the need to exert force on any rope or handle which, in poor weather conditions on deck, can cause serious injury. Even in case of emergency relocking, from a mistaken unlock or otherwise, the handle has been made to move with less effort and can be easily reached with the operation rod.

Since the Wavelock is an intermediate step between manually operated devices and more automated solutions, further developments will include electrically driven actuators with a high degree of ingress protection against water, as well be resistant to degradation from a salt environment.

The move to electric actuation will open new possibilities, such as the integration of wireless antennas, allowing operators to issue lock/unlock commands from anywhere on the ship – using a tablet, for example.

Supplying locks with power will aways be the obstacle to overcome, but it would require vessels to be retrofitted or designed with this in mind. As electric locks become more prevalent onboard container ships, perhaps it will inspire shipyards to account for this in future designs.

Acknowledgements

The Wavelock group would like to thank Perttu Jokinen, Juhana Östberg, Tero Sairanen, and Arto Toivonen from MacGregor for sharing their experience both onboard vessels and from within the industry. Their feedback was invaluable during the development of the Wavelock.

References

[1] Allianz Global Corporate & Specialty (AGCS), "Safety and Shipping Review 2021," Allianz, Munich, Germany, 2021.

[2] P. Zhang, C. Xie and H. Fei, "Twist Lock Unlocking Process Research and Unlocking Fixture Design in container terminals," in *4th International Conference on Computer, Mechatronics, Control and Electronic Engineering (ICCMCEE)*, 2015.

[3] P. Zhang, "Development and Suggestions on Container Twist Lock Handling in Automated Container Terminals," *MATEC Web of Conferences,* vol. 353, 2021.

[4] K. G. N. A. A. L. Panagiotis Panagiotidis, "Shipping Accidents Dataset: Data-Driven Directions for Assessing Accident's Impact and Improving Safety Onboard," *Data,* vol. 129, 2021.

[5] A. J. K. Breteler, "Automatic (un-) locking of twist-locks at maritime containers," Delft University of Technology, Delft, The Netherlands.

[6] T. Baker, "Container Losses from Vessels Using Fully Automatic Twistlocks," North Insurance Management Limited, 2006.

[7] "Automizing the manual link in maritime supply chains? An analysis of twistlock handling automation in container terminals," *Maritime Transport Research,* vol. 2, 22 02 2021.

[8] S. Burthem and A. Brown, "The causes and preventionof container losses," The London P&I Club, London, 2016.

[9] A. Koh, "Shipping Containers Fall Overboard at Fastest Rate in Seven Years," Bloomberg, 21 April 2021. [Online]. Available: https://www.bloomberg.com/news/articles/2021-04-26/shipping-containers-plunge-overboard-as-supply-race-raises-risks. [Accessed 18 March 2022].

People Detection in an Elevator Car Using Computer Vision

Sachin Kundu[1,a], Milan Gautam[1,b], Amali Herath[1,c], Vidar Hermansson[1,d], Panu Kiviluoma[1,e] and Petri Kuosmanen[1,d]

[1] Department of Mechanical Engineering, Aalto University, Finland

[a] sachin.1.kundu@aalto.fi, [b] milan.gautam@aalto.fi, [c] amali.herath@aalto.fi, [d] vidar.hermansson@aalto.fi, [e] panu.kiviluoma@aalto.fi and [d] petri.kuosmanen@aalto.fi

Keywords: elevator, people detection, computer vision

Abstract

There is a need to develop an integrated sensor system in elevator cars to cover as many use cases as possible to address the increasingly stringent laws implemented by governing bodies to ensure passenger safety. This research focused on people detection using computer vision as the first step towards a complete technological solution. Six-phase design methodology was applied. An embedded device was developed with Nvidia Jetson Nano (2GB) and 200° field of view camera. Dataset of 267 images of passengers in real elevator setting was obtained using the device. The performance of existing object detection algorithms - YOLOv5, MobileNetV2SSD and Roboflow AutoML were evaluated by re-training the models with captured image dataset and barrel-corrected image dataset. The performance of YOLOv5 and Roboflow AutoML with barrel-corrected image dataset was similar with promising mean average precision (mAP) whereas mAP for MobileNetV2SSD was subpar. Further improvements should be made to eliminate ghost detections and spurious detections caused due to varying elevator environments with highly reflective surfaces.

Introduction

With the increase of high-rise buildings across the globe due to urbanization, elevators have become an essential day-to-day vertical transportation vehicle. Operation of elevators is governed by stringent safety laws, and adherence to these laws should be clearly demonstrable. To that end, elevator manufacturers are keen to evaluate technological solutions for problems within the elevator car such as overloading, entrapment, panic attacks, and vandalism. While there are several types of sensors developed for each of these use cases, there is still a need to develop an integrated sensor system that can solve as many use cases as possible with the same in-car hardware device.

A wide range of sensors are used in elevators. The sensors can be focused on detecting the state of the elevator itself, thereby assisting in monitoring, fault diagnosis, alarm, and maintenance [1]. These sensors are comprised of speed, vibration, and force sensors. The varying conditions inside an elevator are monitored, for instance by using temperature and humidity sensors, occasionally with the inclusion of smoke detectors [2,3]. People detection in elevators is primarily conducted using infrared sensors and video monitoring. However, the reliability of infrared detection is notably decreased in crowded environments.

Computer vision is an emerging and rapidly growing technology which is already being employed in autonomous driving, surveillance, and safety systems. The real time capabilities of computer vision are being realized, from robotic manipulation to interactive games. This has opened a question on utilization of machine vision for elevators. Significantly more accurate results in people detection in elevators can be achieved by using the surveillance video data combined with machine vision technology, allowing automated processing of the video feed and efficient detection of potentially dangerous situations such as elevator overloading [4].Using a network of low-cost depth cameras has also been explored for people detection and tracking [5]. Traditional computer vision techniques such as Haar like feature has been used for counting passengers inside elevator [6,7]. Calculating the passenger flow in real time using support vector machines (SVM) and YOLOv5 (You Only Look

Once) model has been also studied [8]. A comprehensive study on the applicability of computer vision for both passenger and system protection in elevators, along with the future trends, was also presented [9].

Many of the identified use cases for the elevator sensor system have passenger detection in the elevator car at the root of their solution. Hence, the use of computer vision for people detection in elevator cars is evaluated in this study. Based on the study, it was decided to build an in-car embedded device for people detection, acting as an entry point into a service provider's core network. The developed prototype was used to collect image datasets and three object detection methods were retrained and one was deployed to the edge device utilizing docker containerization platform. Besides being functional, the device is required to be easily updated, without having to visit the site in-person. When existing algorithms are improved, or new sensing abilities are implemented using the same sensor hardware, it should be possible to update the device over the air. Service management, privacy, security, and reliability are identified as challenges in edge environment [10] and therefore, software architecture for an edge device should be designed to overcome these challenges.

Methods

The six-phase design methodology used to develop the device for the purpose of detecting people inside the elevator car is summarized in Fig. 1.

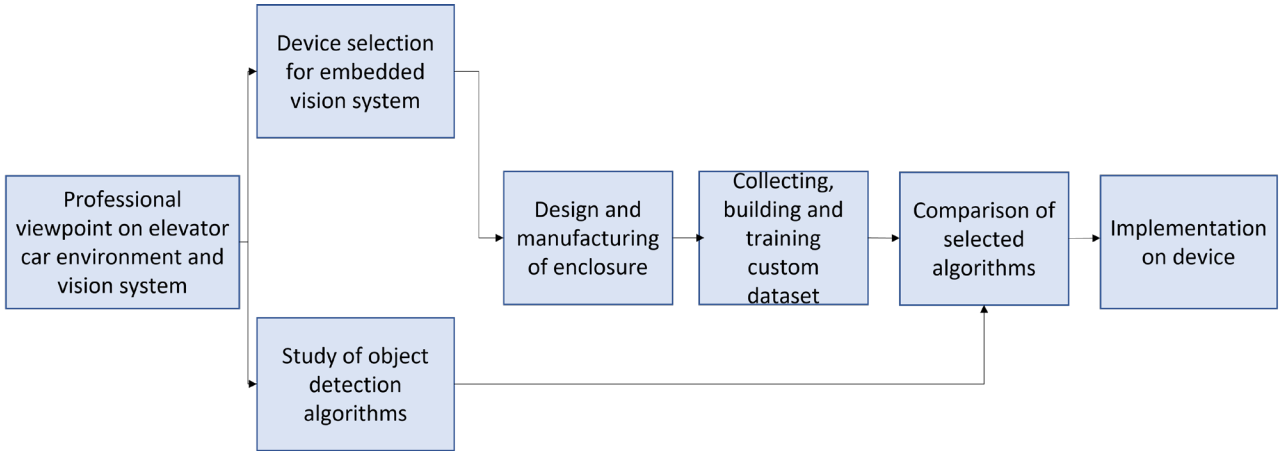

Figure 1. Process used for design and development.

Professional viewpoint on elevator car environment and vision system. Professionals specializing in elevator car design were consulted to obtain their viewpoint on use of computer vision in an elevator car environment. Key challenges identified through discussion are summarized below.

1. Spurious detections due to surface/mirror reflections.
2. Privacy issues.
3. Limited performance of existing object detection algorithms as they are trained on images obtained using a front facing camera (where faces are visible) instead of a top mounted camera.
4. Barrel distortion of images and their effect on object detection performance due to usage of wide field of view lens.
5. Software support for easy updates.
6. Adaptability of hardware to several types of elevator spaces without affecting internal controls of the elevator.

Device selection for embedded vision system. The list of components chosen for the device are as follows:

1. Jetson nano 2GB Developer Kit
2. FOV camera (IMX219-200)

3. Uninterrupted power supply unit
4. DUAL-BAND USB WI-FI ADAPTER – 2

Design and manufacturing of enclosure for the embedded system. The computer vision system is housed inside a 3D printed enclosure consisting of back panel and top enclosure with camera mount as shown in Fig. 2. The enclosure is then mounted on top of elevator car with the camera facing downwards. The optimum mounting location is determined via testing to maximize field of view inside a specific elevator car.

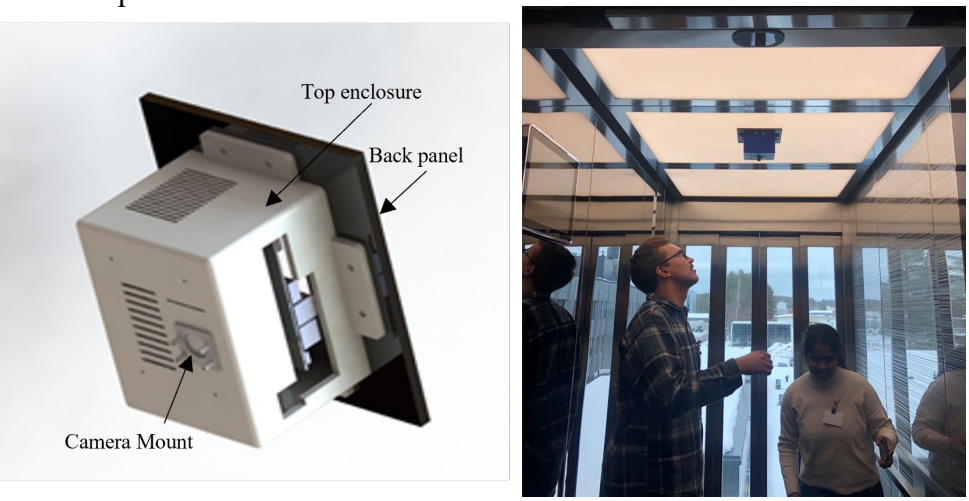

Figure 2. CAD model of the enclosure (left), embedded system mounted in elevator setting (right).

Study of object detection algorithm. The regression/classification-based methods such as YOLOV5 and Mobilenetv2liteSSD were chosen [11,12]. The study was focused on these implementations due to claimed state of art performance, easiness of training and deployment of these algorithms on Jetson Nano. You only look once (YOLO) is a single neural network that can predict bounding boxes and class probabilities directly from full images in one evaluation [13,14]. Additionally, all computation is encapsulated in a single network by Single Shot Multibox Detector [15]. In comparison to previous methods, no object proposals are required and hence the proposal generation and subsequent pixel or feature resampling stage is eliminated, making the network swift and effective.

Collecting, building, and training image dataset. A dataset of 267 images with people and random objects placed within an elevator car was captured from 7 different elevator cars with a ceiling mounted device. The lighting conditions, mirror availability, surface finish of the elevator along with the size of the elevator car were distinctly varied. The device was mounted such that the whole elevator car was captured, and the elevator lobby area was visible depicting the close/open status of the elevator door. The obtained images were annotated to identify people within a bounding box and all other objects were classified implicitly as background. The first set of annotations was obtained using makesense.ai[1] and later imported into Roboflow[2]. A sample of captured image and its annotation is shown in Fig. 3. Converting to different dataset formats is allowed by Roboflow, as expected by the chosen algorithms. Since the images were captured using a wide FOV fisheye lens, these images were also corrected for barrel distortion using OpenCV[3] and a second dataset of corrected images was generated. This corrected dataset was also annotated to identify people and used to train and test another set of models. A sample of the captured image and barrel corrected image is shown in Fig. 4.

[1] https://www.makesense.ai/
[2] https://roboflow.com/
[3] https://opencv.org/

‘

Figure 3.Captured image (left) and image with annotations (right).

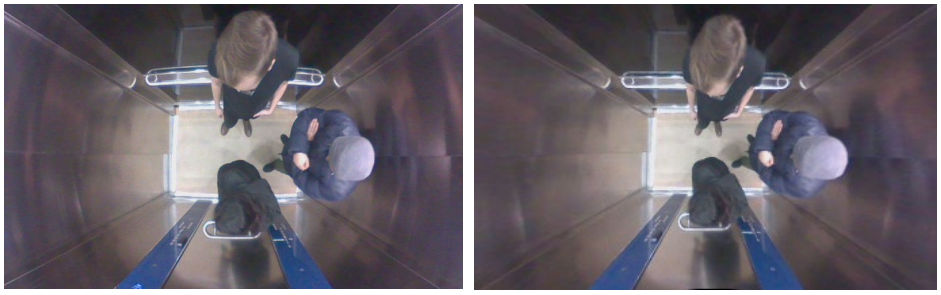

Figure 4. Captured image (left), Barrel corrected image (right).

Training custom dataset using YOLOV5. Transfer learning was used to retrain YOLOV5 on both distorted and corrected dataset using weights for yolov5s, which is a small version suitable for running on embedded devices. The backbone (first 9 layers) of the network were frozen and images were used to finetune the top layers. Hyperparameters as recommended by YOLOV5 authors were used and learning rate was fixed at 0.01 during the whole training.

Training custom dataset using MobileNetV2SSD. Transfer learning was additionally used for training MobileNetV2SSD using the lite version of the pretrained models. In this case the base net was frozen and trained for a total of 50 epochs. A batch size of 5 was used for retraining.

Training custom dataset using Roboflow. Roboflow’s AutoML based object detection framework was used to train models. There was no test time augmentation, image size was fixed at 416x416, and auto orient was applied to the images.

Comparison between trained object detection algorithms. The result obtained by training and testing the image dataset for both captured and corrected on MobileNetv2SSDlite, YOLOv5 and Roboflow AutoML model were compared. Since there are two datasets – captured and corrected, two sets of experiments were conducted. All results are reported at a probability threshold of 0.5. Precision, Recall and Mean Average Precision (mAP) of each of the object detection algorithms were used to evaluate and compare the quality of detection. Precision is a measure of result accuracy whereas recall measures how many results are returned compared to the training labels. The mAP is a score obtained by comparing the ground-truth bounding box to the detected box. The higher the mAP, the more accurate the model is in its detections.

Results

Results obtained from retraining different models are shown in Table 1. For the chosen metrics both YOLOv5 corrected and Roboflow AutoML performed similarly. Due to fundamental trade-off between precision and recall higher scores on both simultaneously could not be obtained. For this application recall was more important than precision as detecting every person was important even though sometimes, the detection were false positives. Corrected dataset performed significantly better

than distorted dataset in all cases. Due to performance of MobileNetv2SSDlite being subpar in captured image dataset it was decided to skip training it also on the corrected dataset.

Table 1. Performance of machine vision models on captured and corrected image dataset.

Image Dataset	Model Name	Precision %	Recall %	mAP %
Captured	MobileNetv2SSDlite	71	60	68
Captured	YOLOv5	82	64	72
Captured	Roboflow custom	87	83	88
Corrected	MobileNetv2SSDlite	No experiment	No experiment	No experiment
Corrected	YOLOv5	81	81	87
Corrected	Roboflow custom	90	86	91

Implementation of selected object detection algorithm in edge device. Reliability of an edge device was of utmost concern. Operation at the edge was required to be hands free as much as possible and perform with low latency. To provide reliable delivery, updates, and frame rates it was decided to run the trained models inside local docker container. For ease of deployment, Roboflow AutoML trained model was deployed on corrected dataset. Jetson compatible container was downloaded from Roboflow, and a custom python script was used to capture the frames from the video feed, barrel correct the image and infer the objects by passing the base64 encoded image to the model running inside the container. The model outputs the objects detected along with their bounding boxes and confidence of detection. The bounding boxes were drawn over detected objects with a confidence of at least 60%.

Discussion

The results shown in Fig. 5 indicate that it is possible to detect persons in an elevator car using a top mounted embedded device. However, the approach still requires further work. In Fig. 5(a) the bounding box includes another person giving wrong person count. In Fig. 5(b) there is a ghost detection due to arm extension. In Fig. 5(c) there is spurious detection due to specular reflections. All these results indicate that there is scope of improvement.

Figure 5. a) Wrong person count. Top-left corner two persons are shown in one bounding box. b) Ghost detection. Extra box is shown in bottom right corner where the hands are extended c) Spurious detection. Extra bounding box marked over the reflection.

The authors suggest the following as further areas of improvement.

1. More images in varied conditions need to be collected with more actors. These models are powerful and given a small dataset they have an ability to memorize the dataset and not generalize. Ideally 1000 images with 10000 labels should be collected.
2. Top mounted camera is one form factor, however more experiments are needed to determine if mounting on other places will provide better results.
3. Hyperparameter tuning and running for more epochs (combined with larger dataset) could give performance boost. Due to lack of time and compute resources we only trained for a limited time with default hyperparameters.

References

[1] Y. Zhou, K. Wang, and H. Liu, "An Elevator Monitoring System Based On The Internet Of Things," *Procedia Comput. Sci.*, vol. 131, pp. 541–544, Jan. 2018, doi: 10.1016/J.PROCS.2018.04.262.

[2] Z. An *et al.*, "Building Elevator Safety Monitoring System Based on the BIM Technology," *J. Phys. Conf. Ser.*, vol. 1939, no. 1, Jun. 2021, doi: 10.1088/1742-6596/1939/1/012026.

[3] Y. Guo, Y. Liu, X. Zhang, and G. Wang, "The Real-Time Elevator Monitoring System Based on Multi-sensor Fusion," *J. Phys. Conf. Ser.*, vol. 2010, no. 1, p. 012182, Sep. 2021, doi: 10.1088/1742-6596/2010/1/012182.

[4] H. Fan, H. Zhu, and D. Yuan, "People Counting in Elevator Car Based on Computer Vision," *IOP Conf. Ser. Earth Environ. Sci.*, vol. 252, no. 3, Jul. 2019, doi: 10.1088/1755-1315/252/3/032131.

[5] T. Tikkanen, "People detection and tracking using a network of low-cost depth cameras School of Electrical Engineering," 2014.

[6] P. Viola and M. Jones, "Rapid object detection using a boosted cascade of simple features," *Proc. IEEE Comput. Soc. Conf. Comput. Vis. Pattern Recognit.*, vol. 1, 2001, doi: 10.1109/CVPR.2001.990517.

[7] H. Liu, Y. L. Qian, Q. Liu, and J. T. Li, "Count passengers based on Haar-like feature in elevator application," *Proc. 7th Int. Conf. Mach. Learn. Cybern. ICMLC*, vol. 2, pp. 1202–1206, 2008, doi: 10.1109/ICMLC.2008.4620586.

[8] J. Zhao and G. Yan, "Passenger Flow Monitoring of Elevator Video Based on Computer Vision," *Proc. 31st Chinese Control Decis. Conf. CCDC 2019*, pp. 2089–2094, Jun. 2019, doi: 10.1109/CCDC.2019.8833248.

[9] S. Lan, Y. Gao, and S. Jiang, "Computer vision for system protection of elevators," *J. Phys. Conf. Ser.*, vol. 1848, no. 1, Apr. 2021, doi: 10.1088/1742-6596/1848/1/012156.

[10] W. Shi, J. Cao, Q. Zhang, Y. Li, and L. Xu, "Edge Computing: Vision and Challenges," *IEEE Internet Things J.*, vol. 3, no. 5, pp. 637–646, Oct. 2016, doi: 10.1109/JIOT.2016.2579198.

[11] Z. Q. Zhao, P. Zheng, S. T. Xu, and X. Wu, "Object Detection with Deep Learning: A Review," *IEEE Trans. Neural Networks Learn. Syst.*, vol. 30, no. 11, pp. 3212–3232, Jul. 2018, doi: 10.48550/arxiv.1807.05511.

[12] M. Sandler, A. Howard, M. Zhu, A. Zhmoginov, and L. C. Chen, "MobileNetV2: Inverted Residuals and Linear Bottlenecks," *Proc. IEEE Comput. Soc. Conf. Comput. Vis. Pattern Recognit.*, pp. 4510–4520, Jan. 2018, doi: 10.48550/arxiv.1801.04381.

[13] J. Redmon, S. Divvala, R. Girshick, and A. Farhadi, "You Only Look Once: Unified, Real-Time Object Detection," in *CVPR 2016*, 2016, pp. 779–788, doi: 10.1016/j.nima.2015.05.028.

[14] G. Jocher *et al.*, "ultralytics/yolov5: v6.1 - TensorRT, TensorFlow Edge TPU and OpenVINO Export and Inference," Feb. 2022, doi: 10.5281/ZENODO.6222936.

[15] W. Liu *et al.*, "SSD: Single Shot MultiBox Detector," *Lect. Notes Comput. Sci. (including Subser. Lect. Notes Artif. Intell. Lect. Notes Bioinformatics)*, vol. 9905 LNCS, pp. 21–37, Dec. 2015, doi: 10.1007/978-3-319-46448-0_2.

Electromechanical Multi-material Extruder for Bioprinting

Kaarlo Mäkelä [1,a] , Ali Hosseini [1,b] , Juho Tevajärvi [1,c] , Verneri Mäntysaari[1,d], Paul Hoffmann [1,e] , Panu Kiviluoma [1,f] and Petri Kuosmanen [1,g]

[1] Department of Mechanical Engineering, Aalto University, Finland

[a]kaarlo.makela@aalto.fi, [b]ali.hosseini@aalto.fi, [c]juho.tevajarvi@aalto.fi, [d]verneri.mantysaari@aalto.fi, [e]paul.hoffmann@aalto.fi, [f]panu.kiviluoma@aalto.fi, [g]petri.kuosmanen@aalto.fi

Keywords: bioprinting, multimaterial extrusion

Abstract

Three-Dimensional (3D) bioprinting using pneumatic based syringe extrusion has limited precision, stemming from leftover pressure, which leads to leftover extrusion when printing is stopped. This study focused on solving this by powering extrusion with electromechanical pistons. To prevent leftover extrusion, force feedback control was developed but not tested. Furthermore, the developed tool contains three syringes which can be operated separately to enable bioprinting with multiple materials which are mixed in a mixing nozzle. Extrusion tests showed that material mixing was successful, but leftover extrusion was not successfully prevented.

Introduction

Three-Dimensional bioprinting is used for bottom-up assembly of biomaterials, biomolecules, and cells. Most printers are limited to the use of a single bioink, which hinders the printing of compositional structures [1]. Different approaches for printing with multiple materials/bioinks have been made. The materials can be mixed actively [2] or passively [3]. Commonly used actuation systems use syringe extruders and screw conveyors. Peristaltic pumps are easy to use but they have strong pulses in their flow [4]. Custom-built syringe extruders are a low-cost option to expensive commercially available syringe pumps [4]. Open-source instructions for syringe extruders for bioprinting have been published [5], and extrusion pressure control has been incorporated successfully in syringe pressure pumps [4]. Brinter's bioprinter offers a modular concept for an easy-to-change dispensing tool [6], which can print three different materials simultaneously. However, it uses a pneumatic based syringe extrusion [7], which has limited precision. Furthermore, retracting material to control over extrusion during high-precision printing is not possible [5].

This study focuses on a multi-material extrusion tool that enables printing of three different materials without the use of pneumatic system. The approach offers an alternative solution to pneumatic systems with more precise printing and quicker stopping due to less leftover-pressure. The actuation is based on stepper motors and pistons, incorporating a force feedback-control to allow stable control of flow as well as adjusting the mixing ratio of the materials.

Methods

System description. Current pneumatic extruders have some leftover pressure which cause over extrusion after the printing is signaled to stop. Reducing this over extrusion for printing with multiple materials is the major requirement for the development of this tool. Piston extruders can be configured such that the piston retracts slightly when extrusion is stopped, which releases the pressure from the material and stops extrusion. Thus, piston actuation was used for the printing module.

Fig. 1 shows the working principle of the printing module. The stepper motors operate the sliders which in turn move the pistons of the syringes. The fluid is guided to a mixing nozzle through a Y-connector connecting the three hoses. For measuring the extrusion force in each piston, load cells were placed between the sliders and the pistons. The tool frame as well as the sliders were constructed

from 3D printed PLA (Polylactic Acid). The frame was attached to the printer with a connector part from Brinter. The slider and the Y-connector were also manufactured by 3D printing.

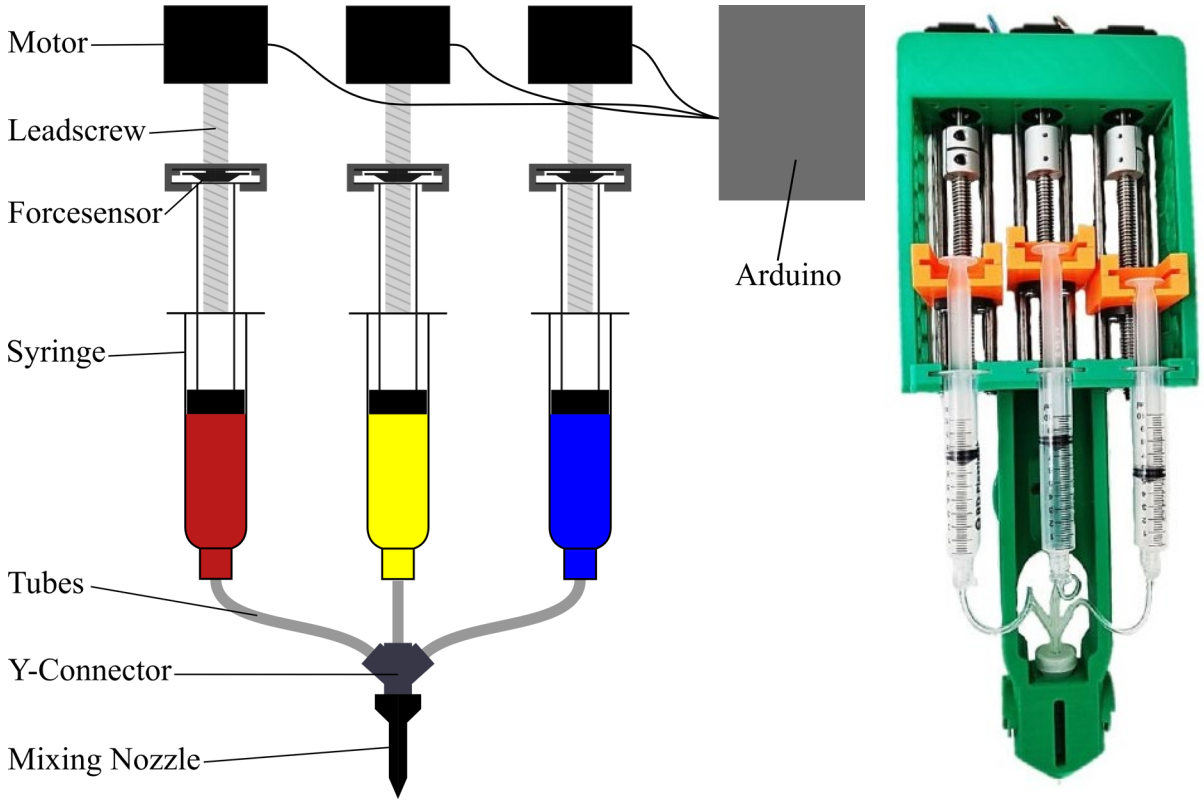

Figure 1. Multi-material printing module.

A PID control loop was developed to control the extrusion force of each syringe. The force feedback-control uses measured piston force values to adjust the stepper motor speeds to match the piston force to the target value. This is demonstrated in Fig. 2.

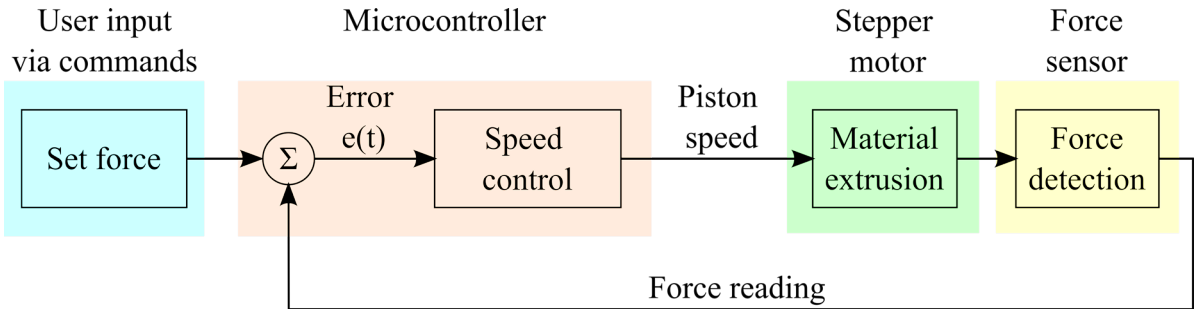

Figure 2. Force-feedback control of the printing module.

For each test, a mixture of powdered sugar and water is used for extrusion because of its similarity to bioinks as a fluid. A water-sugar mass ratio of 1:6,25 (16 m-% water) was used, as this seemed to keep some of its form without seizing in the fluid lines of the tool. The three mixtures were dyed red, green, and white to evaluate mixing performance. Three tests were planned, of which only the first was one conducted, and results reported.

Testing extrusion dynamics. For extrusion dynamic testing (Fig. 3), three straight lines were extruded with material from all three syringes. The tool and the motor were then stopped. Material at the end of the line would indicate a leftover extrusion whereas a constant line would indicate accurate extrusion dynamics.

Testing mixing dynamics. In a mixing test the syringes would be extruded one after another. The resulting prints would be inspected for how quick the transitions are from one material to another. This would test how responsive the system is to mixture changes.

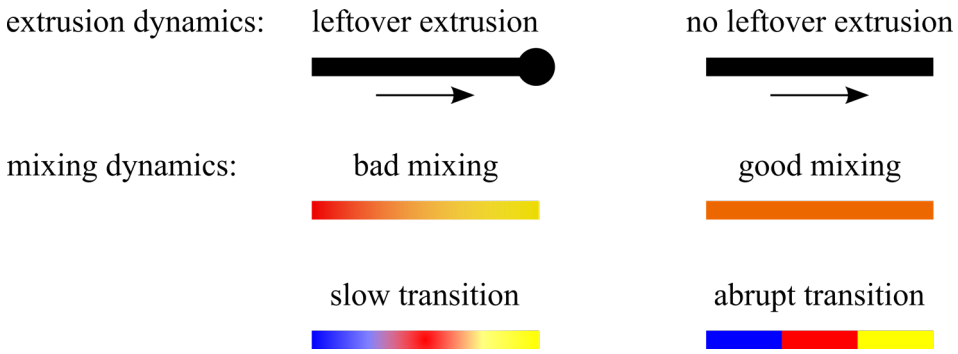

Figure 3. Testing plan for extrusion and mixing dynamics, and markers of extrusion performance.

Testing force feedback-control. Force feedback control can be tested by setting a target force for one syringe. The force readings could be plotted along with the set pressure and time to see how accurately the system reacts.

Results

The testing material proved difficult and inconsistent during testing. Firstly, the mixture is very sensitive to inaccuracies in the ingredient ratio. Varying the water m-% by 0.5 is enough to change the material viscosity noticeably. Secondly, the mixture starts to set as soon as it is mixed. Water evaporates from the mixture when it is in contact with air, and the subsequent reduction in water m-% causes the mixture to solidify locally.

Test extrusion can be seen in Fig. 4. Extrusion was started statically to flow materials to the mixer tip. The green and white syringes managed to push material, albeit while skipping some steps, while the red syringe seized. An attempt was made to manually aid the red material to the mixer tip, but the motor could not produce the necessary extrusion force. This could have been related to the material inconsistency mentioned earlier.

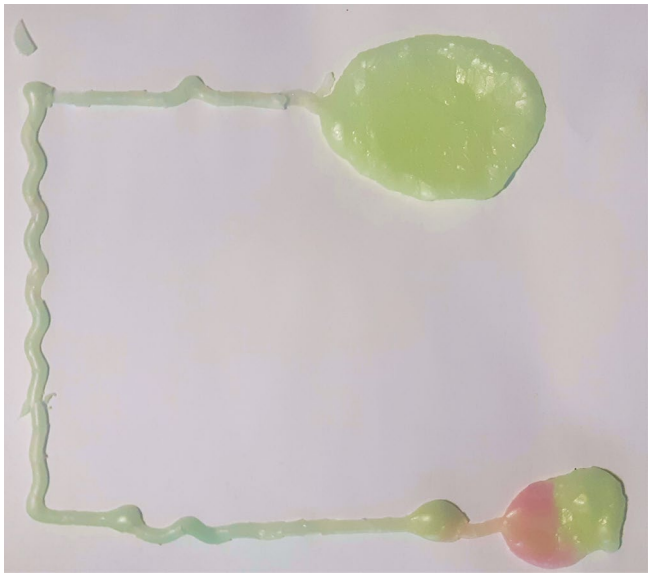

Figure 4. Test extrusion done by moving Brinter from the bottom puddle to the top.

After this, printer movement was started with only two syringes extruding. While the movement consisted of straight lines, the extrusion oscillated from side to side. This was a sign of over extrusion, as the material flowed too much compared to the movement speed of the head.

At the end of the extrusion test, movement was stopped first, and extrusion was ceased afterwards. While the piston retraction was not programmed, it would not have prevented leftover extrusion. Material flowed for about a minute after stopping the motors, even after manually retracting the pistons slightly. Throughout the final extrusion test and during development testing, materials mixed without any visible inconsistencies.

Discussion

The main goals for the multi-material printing module were the ability to mix three materials, control extrusion pressure, stop extrusion quickly, and being compatible with the Brinter. Two of these goals were achieved, while one of them failed and one was not tested due to time constraints. The module mixes materials successfully and produces a consistent extrusion layer. It was also attached to the Brinter and moved successfully, although the extrusion itself was externally powered. Extrusion could not be stopped quickly, and force control was not successfully tested.

One reason for the unresponsive extrusion dynamics could be the large amount of volume beneath the piston. After the syringe, the material must still flow through the hose and the static mixer before extrusion. While the module was designed to have minimal flow volume, this apparently was not enough. A solution to this could be to have the syringes as close to each other as possible and using an even smaller custom-made static mixer.

Another reason is low viscosity of the extrusion material. Throughout testing it was clear that its consistency is a trade-off between risking seizures and over extruding. In the final test, two of the materials were just runny enough not to seize, which was apparent from the motor skipping some steps. This could be solved by either increasing the force output of the piston or by reducing friction losses in the fluid lines, both of which would allow the use of more viscous materials.

While multimaterial extrusion and accurate extrusion dynamics have been studied and accomplished on their own, combining these proved much more difficult than just combining the two. This is because material mixing increases flow volume and friction losses, which directly complicate the extrusion dynamics of the system.

References

[1] W. Liu, Y.S. Zhang, M.A. Heinrich, F.D. Ferrari, H.L. Jang, S.M. Bakht, M.M. Alvarez, J. Yang, Y.C. Li, G.T. Santiago, A.K. Miri, K. Zhu, P. Khoshakhlagh, G. Prakash, H. Cheng, X. Guan, Z. Zhong, J. Ju, G. Zhu, X. Jin, S.R. Shin, M.R. Dokmeci, A. Khademhosseini, Rapid Continuous Multi-Material Extrusion Bioprinting, Advanced materials 29 (2017).

[2] V.G. Rocha, E. Saiz, I.S. Tirichenko, E. García-Tuñón, Direct ink writing advances in multi-material structures for a sustainable future, Journal of Materials Chemistry A 8 (2020) 15646–15657.

[3] A. Miriyev, B. Xia, J.C. Joseph, H. Lipson, Additive Manufacturing of Silicone Composites for Soft Actuation, Journal of Materials Chemistry A 8 (2019) 308–318.

[4] J.R. Lake, K.C. Heyde, W.C. Ruder, Low-cost feedback-controlled syringe pressure pumps for microfluidics applications, PLoS ONE 12 (2017) 1-12.

[5] J.W. Tashman, D.J. Shiwarski, A.W. Feinberg, A high performance open-source syringe extruder optimized for extrusion and retraction during FRESH 3D bioprinting, HardwareX 9 (2021) 1-18.

[6] A. Tong, Q.L. Pham, P. Abatemarco, A. Mathew, D. Gupta, S. Iyer, R. Voronov, Review of Low-Cost 3D Bioprinters: State of the Market and Observed Future Trends, SLAS technology 26 (2021) 333-366.

[7] Information on https://www.brinter.com/product/pneuma-triaxial-pro/ Cited 18.4.2022

Induction Heating of EN 1.4307 Stainless Steel Sheet with Permanent Magnets

Matias Malm[1,a], Joose Haavanlammi [1,b], Markus Kilpiäinen [1,c], Viktor Ketola[1,d], Panu Kiviluoma[1,e] and Petri Kuosmanen[1,f]

[1] Department of Mechanical Engineering, Aalto University, Finland

[a]matias.malm@aalto.fi, [b]joose.haavanlammi@aalto.fi, [c]markus.kilpiainen@aalto.fi, [d]viktor.ketola@aalto.fi, [e]panu.kiviluoma@aalto.fi, [f]petri.kuosmanen@aalto.fi

Keywords: eddy currents, rotating magnets, stainless-steel sheet heater

Abstract

Previous research has shown that pre-heating steel sheet before the cold rolling section in a stainless-steel mill reduces wear on the equipment. In this study, the feasibility of induction heating of EN 1.4307/AISI 304 stainless steel sheet using a rotor fitted with permanent magnets is assessed. Experimental tests have been conducted with stainless steel sheets of different thicknesses. Promising results in induction heating with permanent magnets were seen. It was concluded that more research is to be done regarding optimization of the device before it would be feasible to implement in an industrial scale.

Introduction

Traditional induction heating by running an electric current through a coil and passing a metallic object through the coil has been investigated in the steel industry and it has relatively low efficiency [1, 2] and is prone to breakage due to heat and physical stresses.

Solutions for heating metal sheets with permanent magnets already exist in the aluminium industry [3]. For example, the company GMS has developed and patented such a unit for heating aluminium billets, and it is promoted to be better for the environment as it has better thermal efficiency [9].

The sheet heats up due to changing magnetic fields which create eddy currents and magnetic hysteresis in the metal sheet [4]. Eddy currents are electrical currents induced by changing magnetic field in conductive materials such as metals (Fig. 2). These electrical currents, which in practise are moving electrons in the material, have kinetic energy. While moving the electrons collide with the stationary particles of the conductive material and transform their kinetic energy into thermal energy. This thermal energy is expressed as heat.

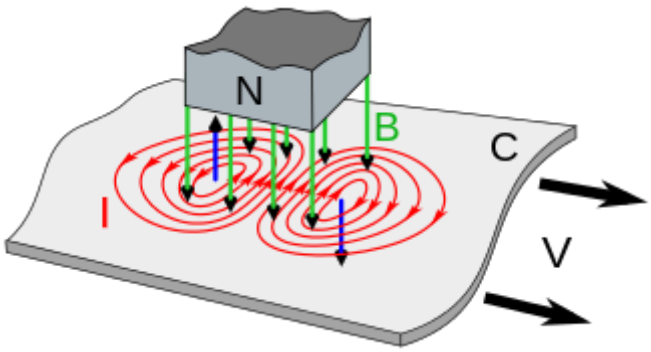

Figure 2. A changing magnetic field (B) of a magnet (N) induce eddy currents (I) in a conductive material (C) [5].

The objective of this study was to induction heat stainless steel to 50-80°C from ambient temperature (+21°C) using a spinning rotor which has permanent magnets fixed on its perimeter. The

purpose of the heating process is to soften the material before the cold rolling section in a stainless-steel mill. The intended placement of the device is shown in Fig. 1. Experimental results have shown that there is a large reduction in rolling forces if the rolled sheets are pre-warmed, which would reduce wear on the equipment [7].

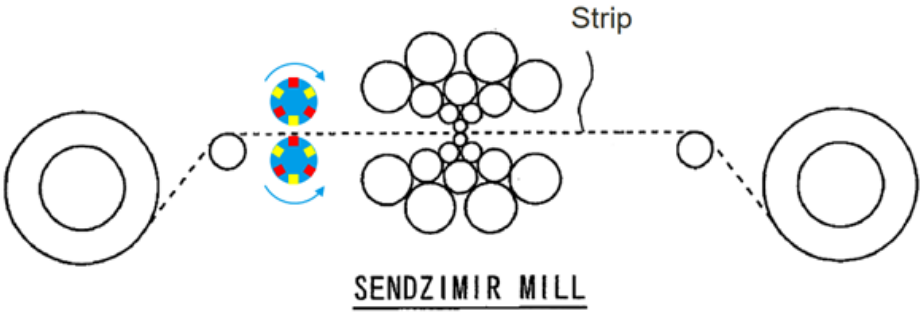

Figure 1. Placement of the induction heating device (blue rotors).

The scientific contribution of this research stems from that previous research in the field had been focused on the properties of induction heating of aluminium, and little research was found on a rotor-based solution for the induction heating. In the previous research, the examined solutions had magnets enclosing the piece to be heated instead of having an external rotor. Numerical simulations on the matter have been published, however, little data from practical experiments was found [6].

Methods

To determine the heating power with induction heating, a testing setup is needed. In Fig. 3 a schematic of the testing setup is seen. The rotor design for these tests is shown in Fig. 4.

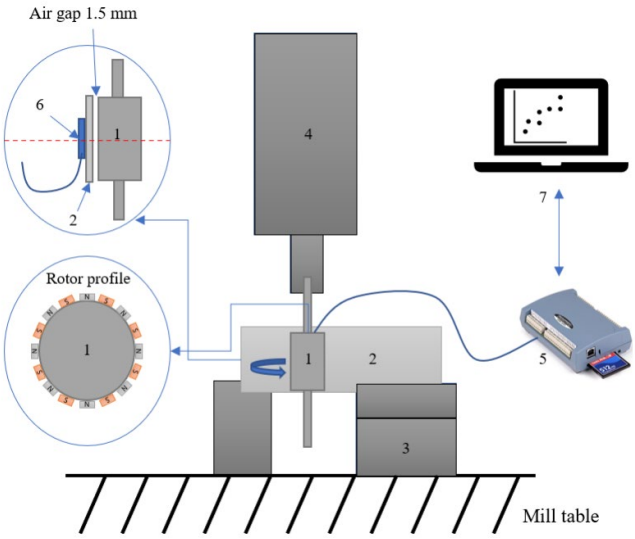

Figure 3. The laboratory test setup.

The essential factors in inducing heat in the metal sheet in an effective way were the air gap between the rotor and the metal sheet, rotor's rotational velocity, magnetic field produced by the permanent magnets and the heat capacity of the sheet material. The constraints of the rotor design were rotor's rotational velocity and the magnets due to machinery, and availability of the magnets. The selected magnets were 80 x 13 x 5mm rectangles which had a magnetic field of 1,42-1,47 T on the surface of the magnet. Due to eddy currents producing Joule heating in the metal, assuming no skin effect occurs during the heating process and the magnet practically being in contact with the

surface of the metal, using the selected magnets, the heating power can be calculated the following equation [8]:

$$\boldsymbol{P = \frac{\pi^2 B_P^2 d^2 f^2}{6k\rho D}} \quad (1)$$

Were

P is induced heating power [W/kg]
B_P is peak magnetic field [T]
d is thickness of sheet [m]
f is frequency [Hz]
k is constant for thin sheet
ρ is material resistivity [Ωmm^2/m]
D is material density [kg/m^3]

Material specification for the stainless steel used in the tests is presented in the Table 1.

Table 1. Specification of the stainless steel used in the tests.

EN 1.4307 specification	
d	1.55 mm and 4 mm
σ	0.73 Ωmm^2/m
D	7900 kg/m^3
c_p	500 J/kgK

Rotor design and configuration can be seen in Fig. 4.

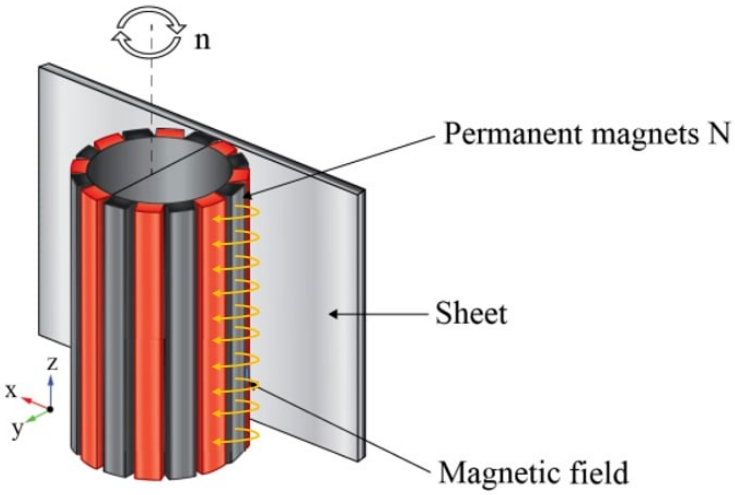

Figure 4. Rotor design and permanent magnets configuration. N is abbreviation of North pole.

The rotor has red and black designated slots (Fig. 4), which indicate that the red is the south pole and the black is the north pole. Magnets on the rotor are positioned in such a way that their polarity shifts, providing a magnetic field with the same orientation as the rotor profile. This is to increase the strength of the magnetic field in this orientation. A magnetic field is created when one pair of south and north form a pole. On the rotor, there are eight poles in total. This implies that at 2500 rpm, the

induced magnetic frequency is equal to the mill frequency multiplied by eight poles, or f = 333 Hz. The rotor is made of aluminum and the magnets are screwed to the rotor with machine screws.

The testing setup (Fig. 3)was implemented on a milling machine that allows the magnetic field to rotate at various speeds, thus changing the frequency f . Table 2 lists the components of the setup referring to the numbering in Fig. 3.

Table 2. Components used in the testing setup.

Number	Description
1	Permanent magnet rotor
2	EN 1.4307 stainless steel sheet (1.55mm and 4mm)
3	Wise
4	Mill (120-2500 rpm)
5	Data logger
6	Termopar temperature sensor
7	PC

From the test the delivered heat into the sheet can be determined as [1]:

$$\boldsymbol{Q = \frac{\Delta T D V c_p}{t}} \tag{2}$$

Where

Q is heating power [W]
ΔT is temperature difference [K]
D is material density [kg/m^3]
V is heated volume [m^3]
c_p is specific heating capacity [J/kgK]
t is testing time [s]

The specific heating power per unit mass is determined as [10]:

$$\boldsymbol{x = \frac{Q}{m}} \tag{3}$$

Where

Q is heating power [W]
m is mass of the volume [kg]

Results

Using Eq. 1, to calculate the theoretical specific heating power, the theoretical heating power for the rotor is seen in Table 3 as P. Assuming no skin effect due to the low frequencies and small sheet thicknesses. This equation also assumes that the remanence of the magnets is what they are specified to, e.g., 1.42 T.

Results for the achieved specific heating power are calculated with Eq. 3. All results based on six tests can be seen in the Table 3.

Table 3. Results for theoretical and actual heating power based on six different tests.

Initial Data
- Testing time is 360 s.
- Heat induced area 10.4 cm^2 (Height = 80 mm and width = 13 mm)
- Table 1 material specification

Test	d [mm]	f [Hz]	Max temp. [°C] *	ΔT [°C]	Air gap [mm]	x [W/kg]	P [W/kg]**
1	1.55	166	30.0	4.51	1.5	6.3	38
2	1.55	333	38.0	12.15	1.5	16.9	154
3	4.00	166	31.2	6.14	1.5	8.5	256
4	4.00	333	40.2	14.93	1.5	20.7	1022
5	4.00	333	31.2	7.76	5.0	10.8	-
6	4.00	333	41.9	16.47	1.0	22.9	-

*achieved after 360 s.
** Theoretical heat output based on Eq.1.

In Fig. 5 it can be seen how the sheet thickness effects the temperature rise.

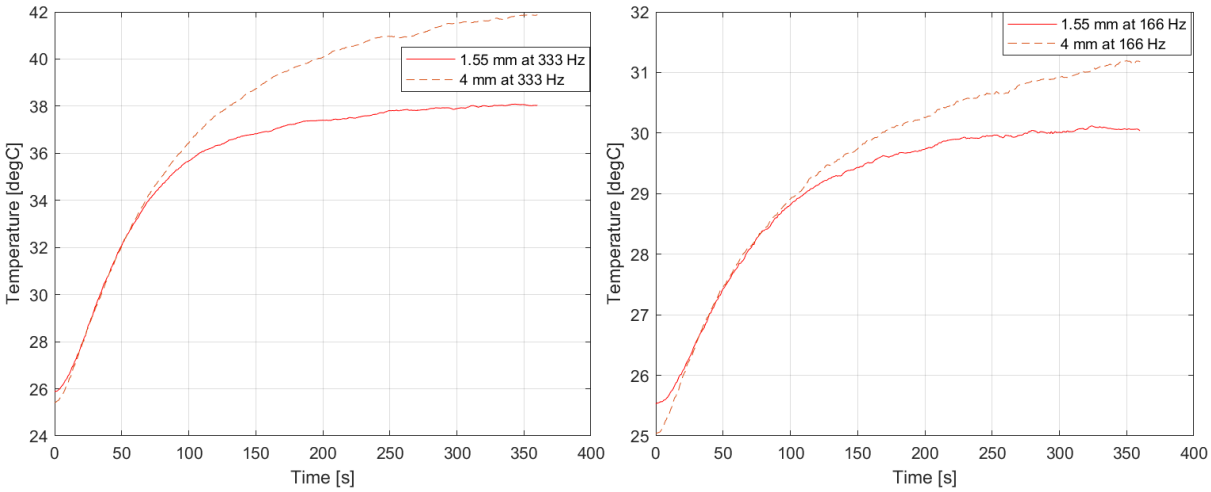

Figure 5. Tests with air gap of 1.5 mm at same frequency with different thicknesses.

In Fig. 6 it can be seen how the frequency effects the temperature rise.

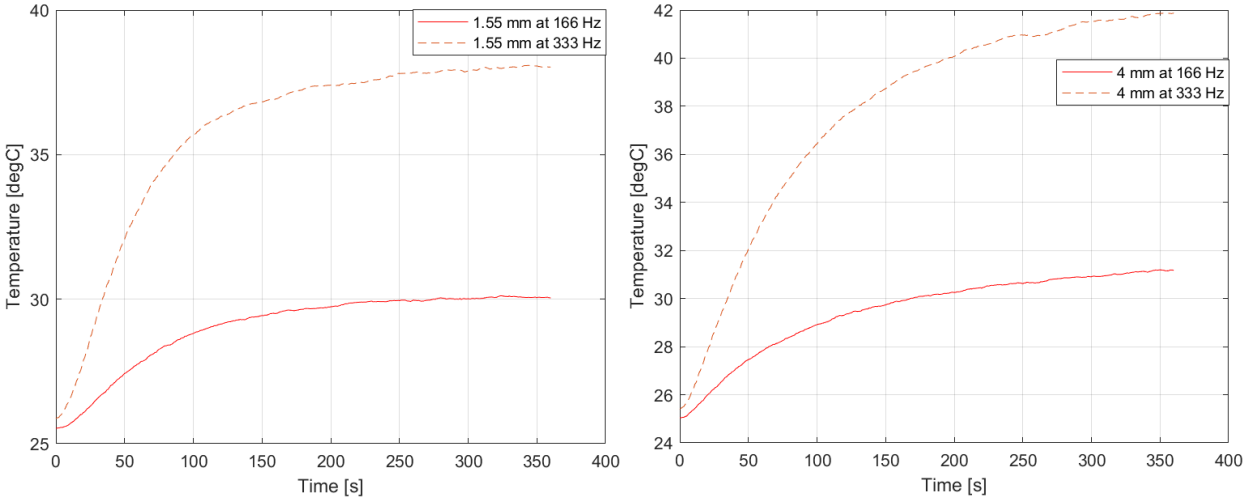

Figure 6. Tests with air gap of 1.5 mm with same thickness but with different frequencies.

It was also investigated how the air gap between the rotor and the sheet affects the heating power. The result of how the air gap affects temperature rise can be seen in Fig. 7.

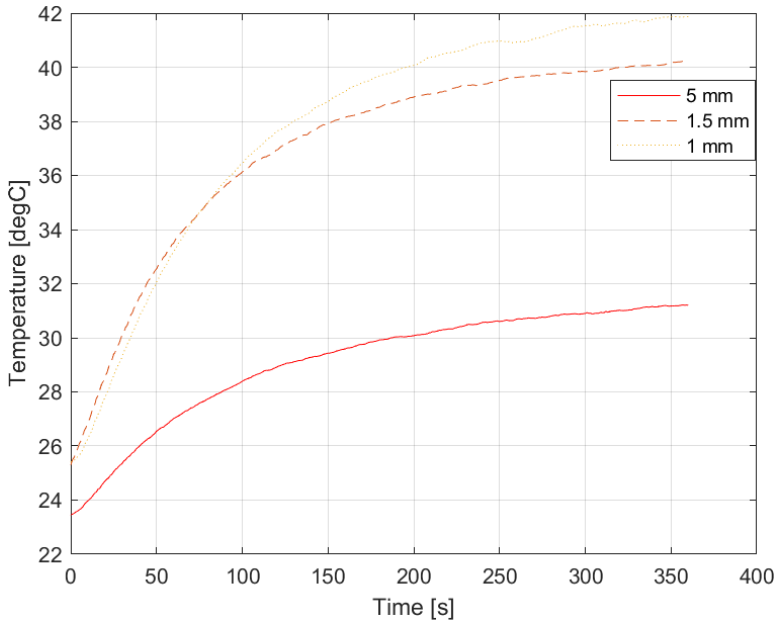

Figure 7. Tests with 4 mm sheet thickness at 333 Hz with different air gaps.

Discussion

Based on the tests, it can be seen that increasing the frequency of the magnetic field has a significant impact on temperature rise and, hence on heating power. Other variables such as sheet thickness and air gap, also had an impact on the heating power. Tests show that induction heating of EN 1.4307 stainless steel is possible. With these tests, the maximum temperature achieved at 333 Hz, 4 mm sheet thickness, 1.0 mm air gap, and testing time 360 s, was 41.9 °C. The ideal temperature for softening metal before cold rolling is between 50 and 80 °C. This implies that the rotor arrangement currently in use is insufficient to meet this target. Considering also that the sheet is moving at the mill, this test result is significantly lower than the required heating demand. Comparison between the theoretical specific heating power P and specific heating power x, indicates that P results may be wrong. If this would be correct to the actual heating power, subtracting potential losses, the heating power could easily be determined with Eq. 1. Which is not the case at the moment. Magnetic field remanence is assumed to be 1.42 T, this could possible be a faulty assumption, thus giving incorrect results.

Future test could be to test Halbach array magnet configuration, which could improve the magnetic field strength. Other tests like higher frequency test could also be interesting. Testing any smaller air gaps could be difficult, because it requires a high tolerance on the rotor roundness and concentricity to the mill. Another future test setup would be to change the magnetic field direction so that it yields an alternating magnetic field instead of the tested setup, which was non alternating. This could also increase the induced heating power [1].

Even though the set temperature value was not reached, and the obtained induced temperature was lower than the preferable value, this study was made to evaluate the feasibility of induction heating using permanent magnets and not to design a working full-scale apparatus. Increasing the diameter of the rotor and adding more magnets on the perimeter of the rotor would increase the induced heat in the sheet but it would also increase the weight of the rotor and the amount of space it needs to operate. Using magnets with greater magnetic field and two rotors with opposing magnets on each side of the sheet would induce more heat and would decrease the diameter of the rotors. This would decrease the amount of area needed for the rotors and their weight which would make them more

practical to handle in an industrial production setting. Using two rotors also may need synchronizing of the magnetic poles.

Permanent magnets are used for heating in aluminum production and due to aluminum´s low electric resistivity the amount of induced heat in the material it is feasible solution in aluminum production. Further study needs to be carried out to determine an optimal design of the rotor or the permanent magnet apparatus in general. Also, a study regarding the overall efficiency of the designed apparatus needs to be carried out in order to compare the results with the current induction heating system which uses induction coils and electric current flowing through the coil.

References

[1] Mach F, Karban P, Doležel I. "Induction heating of cylindrical nonmagnetic ingots by rotation in static magnetic field generated by permanent magnets", *Journal of Computational and Applied Mathematics*. 2012 Dec;236(18):4732–44.

[2] Dughiero F, Forzan M, Lupi S, Zerbetto M. "Induction Heating with Rotating Permanent Magnets: Experimental Results on an Industrial Installation". *2018 19th International Conference of Young Specialists on Micro/Nanotechnologies and Electron Devices (EDM)*. 2018 Jun

[3] Lucia O, Maussion P, Dede EJ, Burdio JM. "Induction Heating Technology and Its Applications: Past Developments, Current Technology, and Future Challenges." *IEEE Transactions on Industrial Electronics* [Internet]. 2014 May [cited 2020 Jun 15];61(5):2509–20.

[4] Brown GH, Moyler CN, Bierwirth RA. "Theory and application of radio-frequency heating." New York Van Nostrand; 1948.

[5] Chetvorno. "Diagram of eddy currents induced in a metal sheet by a magnet." [Internet]. Wikimedia Commons. 2014 [cited 2022 Mar 27]. Available from: https://commons.wikimedia.org/wiki/File:Eddy_currents_due_to_magnet.svg

[6] Nebi O, Fireteanu V. "Multiphysics finite element model of a continuous thin metallic sheets heater with rotating permanent magnets system." *UPB Scientific Bulletin, Series C: Chemistry and materials science*. 2011.

[7] Manninen, T. Senior Research Engineer, Outokumpu Stainless Oy, E-mail conversation 26.1.2022.

[8] Fiorillo, Fausto. Measurement and Characterization of Magnetic Materials. Elsevier Academic Press, 2004, p. 31.

[9] HEH (High Efficiency Heater) Permanent Magnet Heater for Aluminium billets (PATENTED) – Gms-Egt [Internet]. [cited 2022 Apr 6]. Available from: https://www.gms-egt.com/en/riscaldatori-a-magneti-permanenti-heh-high-efficiencyheater-per-le-billette-di-alluminio/

[10] Lupi, Sergio, et al. Induction and Direct Resistance Heating. Cham Springer International Publishing, 2015, p. 266.